Draft version September 1, 2025
Typeset using LaTeX **twocolumn** style in AASTeX631

The most distant γ-ray flare to date: a multiwavelength campaign on the $z = 4.715$ blazar GB6 B1428+4217

Andrea Gokus,[1] Manel Errando,[1] Ivan Agudo,[2] Markus Böttcher,[3] Florian Eppel,[4,5] Juan Escudero Pedrosa,[2,6] Jonas Hessdörfer,[4] Svetlana Jorstad,[7,8] Matthias Kadler,[4] Alex Kraus,[5] Michael Kreter,[3] Felicia McBride,[9] Daniel Morcuende,[2] Jorge Otero-Santos,[2,10] and Jörn Wilms[11]

[1] *Department of Physics & McDonnell Center for the Space Sciences, Washington University in St. Louis, One Brookings Drive, St. Louis, MO 63130, USA*
[2] *Instituto de Astrofísica de Andalucía (CSIC), Glorieta de la Astronomía s/n, 18008 Granada, Spain*
[3] *Centre for Space Research, North-West University, Potchefstroom 2520, South Africa*
[4] *Julius-Maximilians-Universität Würzburg, Fakultät für Physik und Astronomie, Institut für Theoretische Physik und Astrophysik, Lehrstuhl für Astronomie, Emil-Fischer-Str. 31, D-97074 Würzburg, Germany*
[5] *Max-Planck-Institut für Radioastronomie, Auf dem Hügel 69, D-53121 Bonn, Germany*
[6] *Center for Astrophysics | Harvard & Smithsonian, Cambridge, MA 02138, USA*
[7] *Institute for Astrophysical Research, Boston University, 725 Commonwealth Avenue, Boston, MA 02215, USA*
[8] *Saint Petersburg State University, 7/9 Universitetskaya nab., 199034 St. Petersburg, Russia*
[9] *Department of Physics and Astronomy, Bowdoin College, Brunswick, ME 04011, USA*
[10] *Istituto Nazionale di Fisica Nucleare, Sezione di Padova, 35131 Padova, Italy*
[11] *Remeis Observatory & Erlangen Centre for Astroparticle Physics, Universität Erlangen-Nürnberg, Sternwartstr. 7, 96049 Bamberg, Germany*

ABSTRACT

In November 2023, the *Fermi Large Area Telescope* detected a γ-ray flare from the high-redshift blazar GB6 B1428+4217 ($z = 4.715$). We initiated a multi-wavelength follow-up campaign involving *Swift*, *NuSTAR*, the Sierra Nevada and Perkins Observatories, and the Effelsberg 100-m radio telescope. This source, also known as 5BZQ J1430+4204, has shown an anomalous soft X-ray spectrum in previous observations, including possible ionized absorption features or signatures of bulk Comptonization of thermal electrons, which are also detected during the flaring episode. Simultaneous optical data revealed a polarization fraction of $\sim$8% in the R band, confirming that synchrotron emission dominated over thermal emission from the accretion disk. The hard X-ray flux was enhanced during the flare. Modeling of the broadband spectral energy distribution suggests that the high-energy component is dominated by Compton scattering by external seed photons from the accretion disk. The origin of the flare is consistent with the injection of a hard-spectrum electron population in the emission region. With a γ-ray luminosity among the top 5% of flaring events, GB6 B1428+4217 exemplifies a prototypical MeV blazar. Its Compton-dominated SED and extreme luminosity are in line with expectations from the blazar sequence. High-redshift flares like this are critical for understanding jet physics in the early Universe and may improve detection prospects with future missions such as COSI.

Keywords: Blazars (164) — Gamma-ray astronomy (628) — High-redshift galaxies (734) — High energy astrophysics (739) — Relativistic jets (1390) — Radiative processes (2055) — Flat-spectrum radio quasars (2163)

1. INTRODUCTION

Active galactic nuclei (AGN) are powered by accretion onto a supermassive black hole (SMBH). Their radiative output exceeds that of their host galaxy and makes them detectable across cosmological scales. The brightest AGN have generally been classified as quasars, with the most distant one being currently found at a redshift of $z = 7.642$ (Wang et al. 2021). Interestingly, some of these AGN at high redshifts harbor SMBHs with masses exceeding $10^9 M_\odot$ (e.g., Ackermann et al.

dr.andrea.gokus@gmail.com, gokus@wustl.edu

2017; Belladitta et al. 2020; Burke et al. 2024; Ighina et al. 2024), indicating rapid black hole growth in the early Universe, within the first billion years after the Big Bang. Several theories exist for the evolution of these first SMBHs. They could have grown from light seeds with $M_{\rm BH} \leq 10^2 M_\odot$ (e.g., Begelman et al. 2006; Whalen & Fryer 2012), heavy seeds with $M_{\rm BH} \geq 10^4 M_\odot$ (e.g., Bromm & Loeb 2003; Wise et al. 2019), or be the product of a series of hierarchical black hole mergers (e.g., Volonteri et al. 2003). While 'light' black holes are somewhat expected to be created early on as remnants of supernova explosions of the first stars (e.g., Madau & Rees 2001), their accretion rate would need to be consistently above the Eddington limit to reach a billion solar masses within a billion years. However, observational evidence shows that these extreme accretion states tend to be episodic (e.g., Yu & Tremaine 2002). The existence of 'heavy' seeds would relax the growth rate constraints (Bogdán et al. 2024), but their proposed birth mechanisms still present theoretical challenges (e.g., Lodato & Natarajan 2006; Inayoshi et al. 2020; Cammelli et al. 2025).

It is postulated that SMBHs in jetted AGN might grow faster, as powerful jets can enhance the accretion rate (e.g., Volonteri et al. 2011; Ghisellini et al. 2013). Conversely, simulations have shown that rapidly spinning black holes accreting at super-Eddington rates typically prompt the formation of powerful jets (e.g., Sądowski et al. 2014; McKinney et al. 2014). AGN that harbor a jet that we observe close to our line of sight are classified as blazars. Because blazar jets are pointing towards us, their emission appears particularly luminous and variable due to relativistic beaming (Urry & Padovani 1995). As such, blazars are ideal targets to study the conditions and growth of black holes in the early Universe. Compact, flat-spectrum radio emission and detection of high-energy γ-ray radiation are signatures indicating the presence of a blazar jet. In order to assess the jet power, observations in both the X-ray and γ-ray range are crucial to constrain the shape of the high-energy component of a blazar's spectral energy distribution (SED). As their SED typically features two broad non-thermal components, the low-energy component originates from leptonic synchrotron emission, and in the case of high-z blazars covers the radio up to the optical band. X-ray and γ-ray observations cover the rise and fall of the inverse Compton hump, respectively. The peak of the component, which falls in the MeV range, can rarely be measured with current instruments due to the lack of sensitivity to faint AGN in the MeV band. In the high-energy regime, blazars have been detected well above $z > 5$ at X-ray energies (e.g., Sbarrato et al. 2015; Belladitta et al. 2020; Medvedev et al. 2020; Moretti et al. 2021; Sbarrato et al. 2022; Migliori et al. 2023; Wolf et al. 2024; Marcotulli et al. 2025), with the most distant one recently being confirmed at $z = 7$ by Bañados et al. (2024). At γ-ray energies, three sources have so far been detected above $z > 4$ (Liao et al. 2018; Kreter et al. 2020). In the GeV band, detections are scarce due to the large distances as well as the source's redshift shifting the emitted GeV radiation to the MeV band where the *Fermi* Large Area Telescope (LAT) is less sensitive. In addition, γ-ray emission is being attenuated due to extragalactic background light above 10 GeV (Domínguez et al. 2024).

Despite these observational challenges, the detection of new high-redshift blazars is possible during flaring episodes. At X-ray energies, this behavior enabled the recently reported detection of a $z = 6.19$ blazar in the hard X-ray band with *NuSTAR* (Marcotulli et al. 2025). In the γ-ray band, Kreter et al. (2020) showed that high-redshift sources that fall below the detection threshold of time-integrated searches of the *Fermi*-LAT data (Abdollahi et al. 2020) can be significantly detected over a shorter time range of the order of 30 days if the source is flaring. While nearby blazars show shorter typical flaring timescales (days to weeks, e.g., Meyer et al. 2019), the elapsed time in the rest frame of a high-z source is related to the observer's time frame as $t_{\rm rest} = t_{\rm obs}/(1+z)$. At $z \geq 3$, a flare on a time scale of $t_{\rm rest} \sim 7$ days would correspond to $t_{\rm obs} \sim 30$ days. Using this technique, and accounting for random fluctuations that could yield false positives, Kreter et al. (2020) reported detections of two $z > 4$ blazars not previously listed in *Fermi*-LAT source catalogs.

Following this approach, we monitor 80 blazars with $z \geq 3$ from the ROMA-BZCAT catalog (5th edition; Massaro et al. 2009, 2015), looking for a γ-ray signal in the public real-time *Fermi*-LAT data using a 30-day integration window.

In February 2022, our monitoring campaign led to the detection of an exceptional γ-ray outburst from the blazar TXS 1508+572 ($z = 4.31$, Schneider et al. 2007). The flaring activity continued for about six months and the γ-ray luminosity peaked at about $5 \times 10^{49}\,{\rm erg\,s^{-1}}$, placing it among the most luminous flares seen by *Fermi*-LAT (Gokus et al. 2024). Radio follow-up with the with the Very-Long Baseline Array (VLBA) and Effelsberg enabled a measurement of the kinematic speed of the jet (Benke et al. 2024).

In this paper, we report the detection of a γ-ray flare from an even more distant object, the blazar GB6 B1428+4217 ($z = 4.715$; Hook & McMahon 1998). To obtain the crucial quasi-simultaneous data at X-ray

energies as well as data covering part of the synchrotron emission component, we launched a multiwavelength campaign using *Swift*, *NuSTAR*, the Perkins telescope, the T150 telescope at the Sierra Nevada observatory, and the 100-m Effelsberg radio telescope.

In Sect. 2, we describe our analysis of the *Fermi*-LAT data and the source association of the γ-ray detection with the high-z blazar GB6 B1428+4217. We report on the multiwavelength data analysis in Sect. 3, and present the results in Sect. 4. We discuss our findings and conclude with Sect. 5. In this work, we assume a flat cosmology with $H_0 = 67.8\,\mathrm{km\,s^{-1}}$, $\Omega_\lambda = 0.692$, and $\Omega_M = 0.308$ (Planck Collaboration et al. 2016).

2. DETECTION OF A GAMMA-RAY FLARE FROM GB6 B1428+4217

GB6 B1428+4217, which is also known as B3 1428+422 or 5BZQ J1430+4204, is the most distant known γ-ray emitter as already reported by Liao et al. (2018) and Kreter et al. (2020). Two distinct redshift values have been reported in the literature. GB6 B1428+4217 was first identified as a high-redshift radio source in 1998 by Hook & McMahon (1998). Based on a spectrum taken with the 4.2 m William Herschel telescope on La Palma, they derived a redshift of $z = 4.715 \pm 0.010$ by averaging measurements of the Lyα, Si IV/O IV and C IV emission lines. When referring to this work, the rounded up value of $z = 4.72$ is often reported. Later works rely on data from the Sloan Digital Sky Survey (SDSS). As part of an analysis for a large sample, Richards et al. (2009) and Sexton et al. (2022) reported redshifts of $z = 4.665$ and $z = 4.65$ based on photometric data and a Bayesian spectral analysis, respectively. Diana et al. (2022) measured the redshift of their sample of 19 high-redshift blazars using the C IV line and reported $z = 4.71$ for GB6 B1428+4217. For the sixteenth data release of the SDSS quasar catalog, different redshift values using different methods are reported, ranging from $z = 4.64$ to $z = 4.83$, but the most likely redshift after visual inspection is $z = 4.705$ (Lyke et al. 2020). According to Hook & McMahon (1998), the challenges in interpreting the spectrum arise primarily from an asymmetric Ly α line due to absorption and a significant velocity shift between the Ly α and C IV line. This makes the visual inspection of the spectrum that the authors conducted more likely to yield accurate values than the automated analyses done in other papers. In addition, the optical spectrum obtained by Hook & McMahon (1998) has better signal-to-noise ratio compared to the SDSS spectra discussed elsewhere in the literature. Consequently, we conclude that their reported $z = 4.715$ is the most accurate redshift value for GB6 B1428+4217 and we will use this value throughout the paper. The resulting luminosity distance of GB6 B1428+4217 is ∼44.6 Gpc.

GB6 B1428+4217 has been studied across the electromagnetic spectrum, in particular in the X-rays, where it is exceptionally bright. A first observation with the High Resolution Imager (HRI; Truemper 1982; Zombeck et al. 1995) onboard *ROSAT* confirmed its quasar nature (Fabian et al. 1997), with subsequent observations resolving intrinsic variability in the X-ray (Boller et al. 2000) and radio bands (Fabian et al. 1999). Based on ASCA data revealing a hard X-ray spectrum, GB6 B1428+4217 was proposed to belong to the class of MeV blazars (Fabian et al. 1998). Boller et al. (2000) found excess absorption using the Position Sensitive Proportional Counter (PSPC; Truemper 1982) instrument onboard *ROSAT*, which was also detected in a *BeppoSax* observation (Fabian et al. 2001), and suggested that it originates from a highly-ionized nuclear absorber with $N_H \sim 10^{23}\,\mathrm{cm^{-2}}$. Using the *Chandra* observatory and the Very Large Array (VLA), Cheung et al. (2012) reported extended X-ray and radio emission from one of its jets. In 2005, GB6 B1428+4217 exhibited a radio flare that was not accompanied by an increase in X-rays (Worsley et al. 2006) nor the emergence of a new jet component (Veres et al. 2010). However, long-term monitoring over 22 years with VLBA revealed superluminal speed of its jet (Zhang et al. 2020). The detection of γ-ray emission associated with GB6 B1428+4217 based on the observation of multiple subthreshold flares seen by *Fermi*-LAT was first reported by Liao et al. (2018) and then confirmed by Kreter et al. (2020).

2.1. *Analysis of Fermi-LAT data*

Following the approach of Kreter et al. (2020) we search for significant γ-ray emission from high-redshift blazars in the real-time public LAT data using a 30-day integration window. In November 2023, our pipeline indicated the presence of a γ-ray excess from the direction of GB6 B1428+4217 in the MJD 60253.0–60283.0 time window.

After the inital trigger, we performed a dedicated analysis of the LAT data. To extract the data, we use ScienceTools Version 2.2.0 and `fermipy` version 1.3.1 (Wood et al. 2017) and select all events between 100 MeV and 300 GeV within a region of interest (ROI) of 15° radius centered at the γ-ray coordinates of the source to be analyzed. We select events of the `SOURCE` class and apply the `DATA_QUAL>0` and `LAT_CONFIG==1` filters. In order to avoid contamination by photons originating from any Earth-limb effects, only events entering LAT with a maximum zenith angle of 90° are consid-

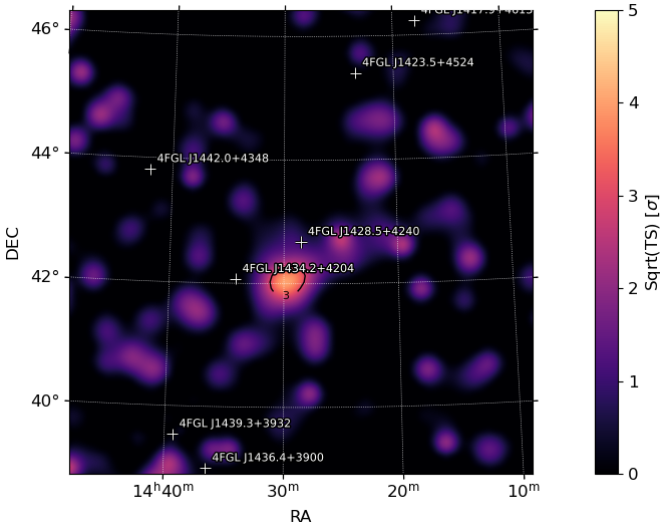

Figure 1. Cut-out of the resulting TS map for an analysis of the ROI without including a new γ-ray source. The signals from known sources have been subtracted. An excess remains that is positionally coincident with the blazar GB6 B1428+4217.

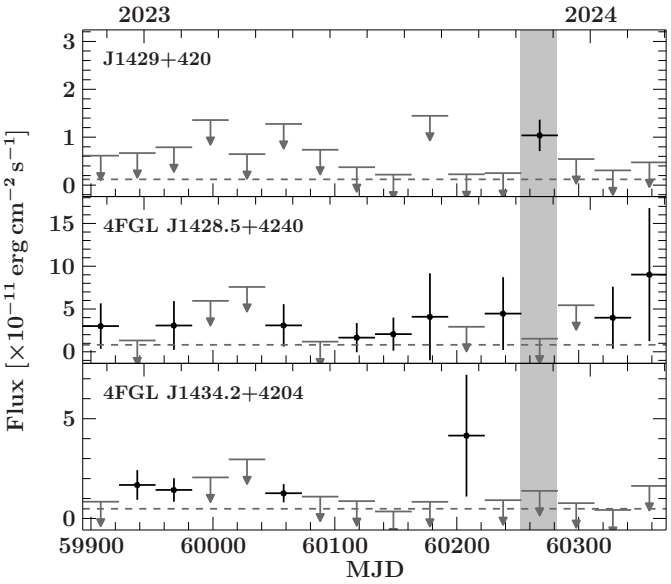

Figure 2. Gamma-ray light curves of J1429+420 (*top*), 4FGL J1428.5+4240 (*middle*), and 4FGL J1434.2+4204 (*bottom*). Each bin covers a time range of 30 days. Upper limits at the 2σ uncertainty are shown for bins that contain a low source detection significance of TS<9. The dashed horizontal line marks the average 4FGL flux of the two known γ-ray sources, and the 15-year average flux derived for the new source J1429+420.

ered. We use the post-launch instrument response functions `P8R3_SOURCE_V3`. We model the ROI considering all sources within 20° of the ROI center that are listed in the 4FGL-DR4 catalog (Ballet et al. 2023) and include isotropic (`iso_P8R3_SOURCE_V3_v1.txt`) and Galactic (`gll_iem_v07.fits`) diffuse γ-ray emission. The method to model *Fermi*-LAT data is a maximum likelihood analysis that expresses the significance of a source in the model via the test statistic value $\mathrm{TS} = 2\Delta\log(\mathcal{L})$. The test statistic thereby determines the difference in likelihood $\mathcal{L}$ between a model with and without a source (Mattox et al. 1996).

The 4FGL catalog lists two γ-ray sources, 4FGL J1428.5+4240 and 4FGL J1434.2+4204, within 1° from GB6 B1428+4217. After optimizing our model for the ROI, we perform a likelihood fit, leaving the normalization and spectral parameters of 4FGL J1428.5+4240 and 4FGL J1434.2+4204 free. The normalization parameters for the Galactic and isotropic diffusion emission components as well as for point sources within 5° of the ROI are also left free. Sources with TS < 1 that are not within 3° from the center are excluded from the model. The signals of 4FGL J1428.5+4240 and 4FGL J1434.2+4204 have a low significance with TS ~ 1 and TS ~ 5, respectively. The resulting TS map (see Fig. 1) shows an excess that cannot be satisfactorily explained by an enhanced γ-ray flux from known 4FGL sources, indicating the presence of an additional γ-ray source.

We then proceed to redo the same analysis with a new source located at the position of the observed gamma-ray excess added to our model. To extract the signal from this new source, we fix the properties of all γ-ray sources in the ROI after the initial optimization (using `optimize`) without the new γ-ray source. This is necessary to avoid fitting a model with too many free parameters that cannot be effectively constrained by the data. In addition, for the closest neighboring sources, 4FGL J1428.5+4240 and 4FGL J1434.2+4204, we set the spectral parameters to their 4FGL value instead of using the optimized value. We choose this approach due to the spectral parameters of both sources agreeing with the 4FGL value and the possibility of low-energy photons originating from the γ-ray excess being associated with the neighbors due to the large point spread function ($> 1°$) at $E < 1$ GeV. In particular, 4FGL J1434.2+4204 is a flat spectrum radio quasar with a soft spectrum similar to what we would expect from a high-z blazar, which could create confusion at the lowest energies.

Using the *fermipy* `localize` function, we find that the new gamma-ray source, J1429+420, is located at $\alpha = 217.41° \pm 0.08°$, $\delta = +42.04° \pm 0.08°$ with a localization uncertainty of $11.6'$ at 95% confidence level. The null hypothesis (i.e., the new source is not present) is rejected with a TS = 18.8, corresponding to a significance

of $\sim 4.3\sigma$. The spectrum of the source is a power law with a photon index of 2.1 ± 0.3 and a flux of $(1.4\pm0.8)\times 10^{-8}\,\mathrm{ph\,cm^{-2}\,s^{-1}}$, or $(1.3\pm0.6)\times10^{-11}\,\mathrm{erg\,cm^{-2}\,s^{-1}}$. We acknowledge that the resulting significance is below the standard TS $\geq$ 25 used for reporting the detection of a new source. However, GB6 B1428+4217 has already been established as a γ-ray source based on recurring flare detections that individually appear at TS $>$ 9 (Liao et al. 2018; Kreter et al. 2020). The γ-ray analysis reported here, together with the multiwavelength data collected contemporaneously, enables us to provide the best picture so far of the SED of this object.

In order to derive constraints for the γ-ray emission before the detection of the flare, we perform a standard analysis using the 15-year LAT dataset (MJD 54683–60250) and add a point source at the best-fit coordinates derived for J1429+420. In our analysis covering this time range, we detect an additional new γ-ray source about 6° from J1429+420, at $\alpha = 215.672°$ and $\delta = 48.005°$, which is included in our analysis, and for which a follow-up analysis is under way for a future publication. The γ-ray excess from GB6 B1428+4217 in the 15-year LAT data has a significance of TS = 15.3, corresponding to $\sim3.9\sigma$. With a photon index of 3.1 ± 0.3, the spectrum is significantly steeper than during the flaring state. The derived flux is $(4.0\pm1.5)\times10^{-9}\,\mathrm{ph\,cm^{-2}\,s^{-1}}$, or $(1.2\pm0.4)\times10^{-12}\,\mathrm{erg\,cm^{-2}\,s^{-1}}$.

In addition, we compute 30-day binned light curves of J1429+420 and both neighboring sources over a time range of $\sim$ 15 months. The light curves shown in Fig. 2 illustrate that the emergence of J1429+420 is not coincident with increasing flux behavior in either of its neighboring sources.

2.2. *Source association with the high-redshift blazar GB6 B1428+4217*

The large localization uncertainty of the new γ-ray source of 11.6′ requires a multiwavelength approach to determine the most likely counterpart of the detected γ-ray source. We use publicly-available sky maps from *XMM-Newton* (Watson et al. 2009) and the LOFAR two-metre sky survey (DR2; Shimwell et al. 2022), shown in Fig. 3 (upper panels), to search for potential X-ray and radio counterparts within the 95% uncertainty region of J1429+420. In the *XMM-Newton* X-ray image, which covers the complete uncertainty region, two bright sources are visible: the brighter one is the blazar GB6 B1428+4217 (α = 217.598923°,δ = 42.076803°), while the other prominent X-ray source is the quasar 2MASS J14302580+4159572 (α = 217.607442°, δ = 41.999065°) located about 4.7′ south of GB6 B1428+4217. In the radio image, more objects are visible, with the brightest again being GB6 B1428+4217. There is no radio counterpart for 2MASS J14302580+4159572. A radio source is close to the best-fit γ-ray coordinates, however, the X-ray source with which it has been associated is too weak to be visible in the *XMM-Newton* map. The *Swift*-XRT map (Fig. 3, bottom left panel) taken as part of our follow-up campaign also reveals GB6 B1428+4217 and 2MASS J14302580+4159572 as the only two prominent X-ray sources within the localization error. In the hard X-rays, about 20% of the uncertainty area is covered, which includes both the positions of GB6 B1428+4217 and 2MASS J14302580+4159572. While GB6 B1428+4217 appears as a bright source, only a slight excess is visible for 2MASS J14302580+4159572. Hence, we conclude that the most likely counterpart for J1429+420 is indeed GB6 B1428+4217. To probe the association with the Bayesian association method described in Abdo et al. (2010), we use our best fit coordinates, uncertainties, and ellipse position angle of 142.1° with the prior probability value for the BZCAT (0.308). Our calculation yields a probability of 0.87 for GB6 B1428+4217 being the counterpart of J1429+420.

3. MULTIWAVELENGTH OBSERVATIONS AND DATA ANALYSIS

3.1. *X-ray data*

We model all X-ray spectra with the Interactive Spectral Interpretation System (ISIS, Version 1.6.2-51 Houck & Denicola 2000) using `vern` cross sections (Verner et al. 1996) and the `wilm` abundances (Wilms et al. 2000) for absorption by the interstellar medium. The Galactic foreground absorption for GB6 B1428+4217 is $N_{\mathrm{H}} = 9.29\times10^{19}\,\mathrm{cm^{-2}}$ according to the HI 4π survey (HI4PI; HI4PI Collaboration et al. 2016). All uncertainties of the best-fit parameters are given at the 1σ confidence level.

3.1.1. *Swift-XRT*

We extract all available *Swift*-XRT data in order to characterize the X-ray flux variability from GB6 B1428+4217. This blazar has been observed by *Swift* on singular instances in 2008, 2013, 2014, and 2023, while in 2021 and 2024 denser monitoring is available. The latest monitoring data set is connected to our follow-up campaign after the detection of the γ-ray flare. We extract spectra and corresponding response files using HEAsoft (V6.33.2; Nasa High Energy Astrophysics Science Archive Research Center (Heasarc) 2014) and the XRTDAS[1] pipeline (v 3.7.0) with CALDB version

[1] https://swift.gsfc.nasa.gov/analysis/xrt_swguide_v1_2.pdf

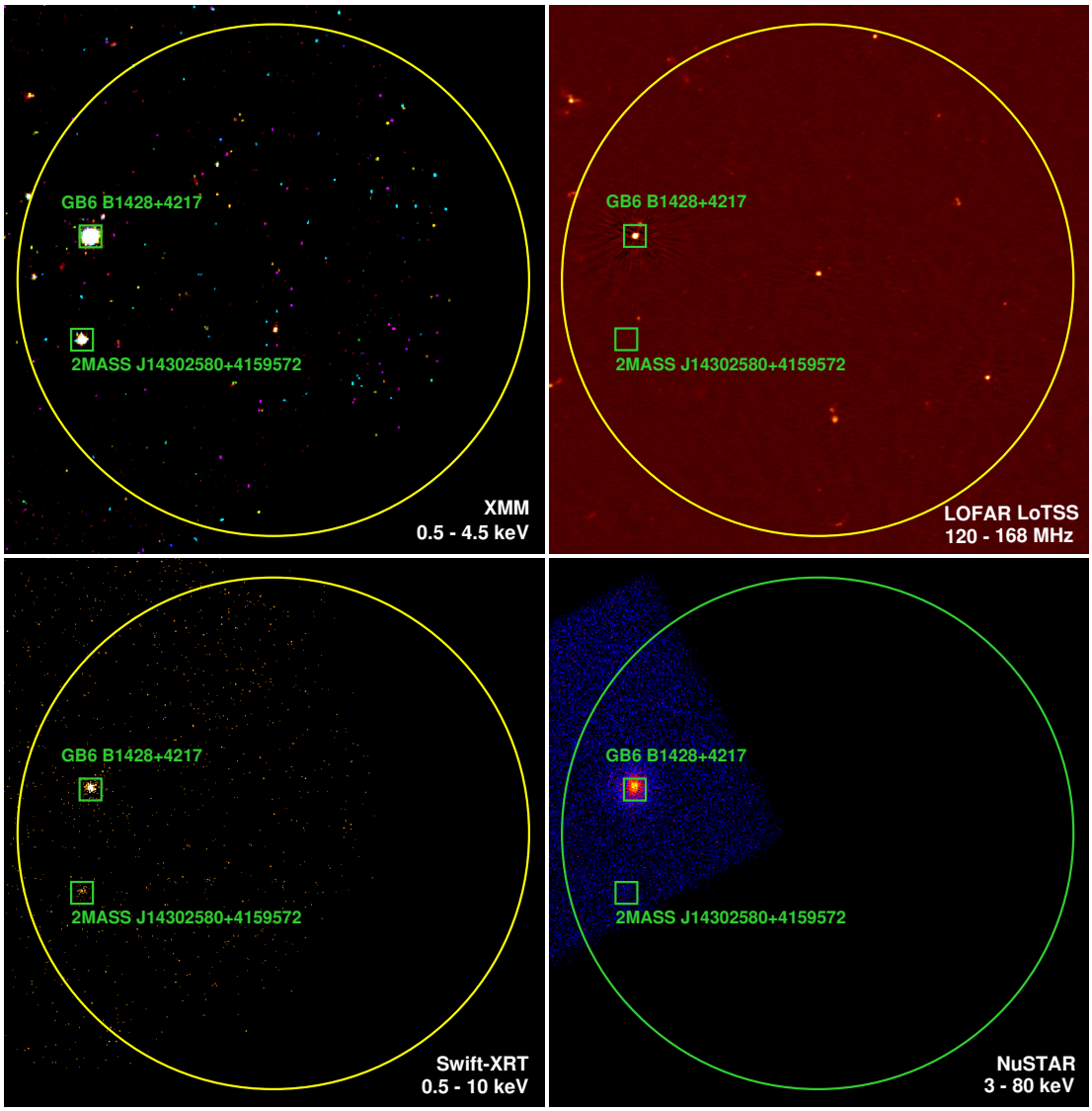

Figure 3. *Upper panels:* Maps from *XMM-Newton* (Watson et al. 2009) and the LOFAR LoTSS (Shimwell et al. 2022). *Lower panels: Swift*-XRT (ObsID: 00016413012) and *NuSTAR* (ObsID: 90901634002, FPMA) maps from observations taken as part of the multiwavelength campaign to follow-up the detection of J1429+420. Squares show GB6 B1428+4217 and 2MASS J14302580+4159572 centered on their radio and optical coordinates, respectively. The width of each map spans $\sim 12'$, with the region of uncertainty being shown as a circle with a radius of $11.6'$.

20240522. All observations have been performed in Photon Counting mode. As source extraction region, we chose a circular region of $40''$ centered on the source coordinates ($\alpha = 217.59827°$, $\delta = 42.07589°$), while the background region is chosen as an annulus with an inner radius of $50''$ and an outer radius of $150''$ centered on the same coordinates.

3.1.2. *NuSTAR*

We obtained a target-of-opportunity observation with *NuSTAR* on 2023 Dec 09 (ObsID: 90901634002) for a total exposure time of 58 ks. For the data extraction, we used the standard procedures with `NUSTARDAS`[2] (v 2.1.2) and CALDB version 20231205. Using `nuproducts`, we extract response files and spectra of the source from a circular region with a radius of $60''$ and centered on $\alpha = 217.5997°$ and $\delta = 42.0710°$ for both Focal Plane Modules A and B (FPMA, FPMB). For the extraction of the background spectra, we chose an annular region

[2] https://heasarc.gsfc.nasa.gov/docs/nustar/analysis/nustar_swguide.pdf

Table 1. Optical data taken with the Sierra Nevada Observatory (SNO) and the Perkins telescope (PTO).

Date	MJD	Magnitude		Observatory
		R band [mag]	I band [mag]	
2023-12-12	60290.2	20.50 ± 0.30	19.21 ± 0.23	SNO
2023-12-14	60292.2	20.53 ± 0.25	19.44 ± 0.20	SNO
2023-12-16	60294.2	20.58 ± 0.21	19.25 ± 0.13	SNO
2023-12-19	60297.2	20.67 ± 0.12	19.54 ± 0.24	SNO
2023-12-20	60298.2	20.25 ± 0.29	19.50 ± 0.40	SNO
2023-12-22	60300.2	20.42 ± 0.09	19.64 ± 0.15	SNO
2024-01-10	60319.5	20.60 ± 0.07	-	PTO

around the source coordinates with inner and outer radii of 60″ and 120″, respectively.

In addition, we extract spectra from an earlier observation of GB6 B1428+4217 that was taken in July 2014 (ObsID: 60001103002) using the same procedure and tools. For both FPMs, the extraction region of the source spectra is centered on slightly different coordinates (RA = 217.5995° and Decl. = 42.0760°) but the same radius for the region is chosen. The background spectra are extracted from circular regions in a source-free region with a radius of 120". The exposure of this observation is 49 ks.

3.2. *Optical*

In December 2023, we monitored GB6 B1428+4217 with the 1.5-m telescope at the Sierra Nevada Observatory and obtained optical photometry in the R and I band. In addition, we measured the optical polarization of the source in the R band with the 1.83 m Perkins telescope. We note that due to the high redshift of this blazar ($z = 4.715$), optical data with wavelengths shorter than 694.8 nm / 4.315×10^{14} Hz are affected by absorption of the Lyman-alpha forest ($\lambda_{\rm rest} = 121.57$ nm).

3.2.1. *Sierra Nevada Observatory*

Optical photometric observations of GB6 B1428+4217 were also performed from Sierra Nevada Observatory (Granada, Spain). These observations were carried out with the 1.5-m T150 telescope in the optical R and I bands between 2023 December 12 and 22, within the blazar optical monitoring program TOP-MAPCAT (Agudo et al. 2012). These data were reduced and analyzed with the automatic photo-polarimetric analysis pipeline IOP4 (see Escudero Pedrosa et al. 2024b,a). We list our results in Table 1. For 2023 December 22, we obtained three observations taken about 20 to 30 minutes apart each. Since within uncertainties the measured magnitudes agreed with one another, we list the average magnitude calculated using the inverse variance weighting method in our results table. We do not find noticeable variation of the source during the monitoring period in December 2023 and it also does not appear brighter than an archival observation in the R band listed in 5BZCAT(Massaro et al. 2009).

3.2.2. *Perkins telescope*

We performed photometric and polarimetric observations of the quasar GB6 B1428+4217 on 2024 January 10. The observations were carried out in R band (λ_{eff} =635 nm) at the 1.83 m Perkins telescope (PTO, Flagstaff, AZ, USA) using the PRISM camera[3] equipped with a polarimeter with a rotating half-wave plate. The polarimetric observation involved three series of Stokes parameters Q and U measurements. Each series consisted of four measurements at instrumental position angles (P.A.s) 0°, 90°, 45°, and 135°, with a 300 s exposure at each P.A. Each Stokes parameter was averaged over series, with the scatter across the series used to estimate an uncertainty. The PRISM camera has a field of view of $14' \times 14'$. This allows us to use field stars to perform both interstellar and instrumental polarization corrections of the Stokes parameters. For absolute calibration of the polarization P.A., we used polarized stars from Schmidt et al. (1992). After all corrections we have obtained a final degree of polarization P = (8.6±3.0)% and electric-vector P.A. $\chi = (-49.5 \pm 9.8)°$ for the quasar GB6 B1428+4217.

We have determined magnitudes in R band of three comparison stars, A, B, and C (see Fig. 4), in the field of GB6 B1428+4217 using differential photometry with comparison stars 1, 2, 3, and 4 in the field of blazar 1ES 1426+428 with known magnitudes (Smith et al. 1991), which is close to the field of GB6 B1428+4217. 1ES 1426+428 was observed with three exposures of 60 s each before and after observations of GB6 B1428+4217. GB6 B1428+4217 was observed with three exposures of 300 s. As a result of these observations, we have determined the R band magnitudes of the stars in the field of GB6 B1428+4217 as follows: A=15.121 ± 0.005, B=15.721 ± 0.006, C= 16.674 ± 0.004. These stars were used to estimate the magnitude of the quasar in the R band on 10 January 2024 to 20.60 ± 0.07.

3.3. *Radio data*

We observed GB6 B1428+4217 with the Effelsberg 100-m telescope on 15 December 2023 and 14 January 2024. These observations covered a range of frequencies from ∼2 GHz to ∼25 GHz. We performed cross-scans

[3] https://www.bu.edu/prism/

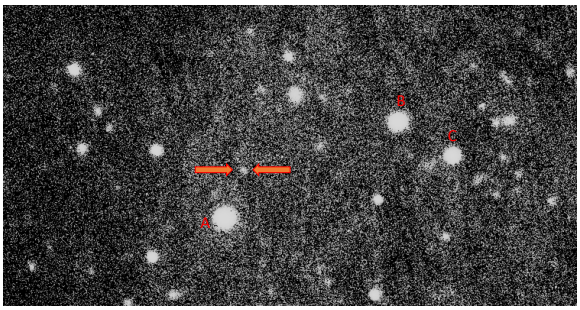

Figure 4. Field of GB6 B1428+4217 in R band in polarized light, labels show the comparison stars A, B, and C.

Table 2. Radio measurements taken with the 100-m radio telescope Effelsberg.

Date	MJD	Frequency [GHz]	Flux density [mJy]
2023-12-15	60293.5	4.85	111 ± 11
		6.55	105 ± 2
		15	176 ± 3
		21.4	163 ± 4
2024-01-14	60323.5	2.35	110 ± 1
		4.85	109 ± 1
		10.45	144 ± 2

over the position of the point-like source in azimuth and elevation. The data are then averaged, undergo a quality-check by a semi-automatic pipeline, and are corrected for pointing offsets, atmospheric opacity and elevation-dependent gain errors. Our calibration source is the standard calibrator 3C 286. The details of the observation and data reduction process are described in Eppel et al. (2024). While we followed the same strategy, we added observations at lower frequencies. We list the fluxes from both observing epochs in Table 2. During both observations, we find flux densities of ∼110 mJy at lower frequencies (2–5 GHz), while the flux densities increase at higher frequencies up to 176 mJy at 15 GHz, resulting in a slightly inverted spectrum. Compared to archival data presented in Worsley et al. (2006), the measured radio fluxes are comparable to a non-flaring state in the radio band.

4. RESULTS

4.1. *Gamma-ray spectra*

Even though we average over ∼15 years of LAT data, the signal determined for our long-term spectrum and the derived flux and photon index may be contaminated by flaring episodes. Our best fit results for the

Table 3. Gamma-ray best fit results.

MJD	$\mathrm{Flux}_{0.1-300\,\mathrm{GeV}}$ $[10^{-8}\,\mathrm{ph\,cm^{-2}\,s^{-1}}]$	Γ	$\mathrm{L}_{0.1-300\,\mathrm{GeV}}$ $[10^{48}\,\mathrm{erg\,s^{-1}}]$
60253 – 60283	1.4 ± 0.8	2.1 ± 0.3	3.9 ± 3.8
54683 – 60250	0.40 ± 0.15	3.1 ± 0.3	2.0 ± 0.8

γ-ray spectra are listed in Table 3. The flux increase during the flaring epoch in 2023 in comparison to the flux derived from the long term measurement is a factor of ∼3.5, however due to the large uncertainties, a 22% chance remains that those fluxes are in agreement with one another. The blazar seems to exhibit a harder-when-brighter behavior found in the majority of FSRQ. The difference in photon index is of the order of 2.4σ, that is, only a small probability of 1.8% that the γ-ray photon index of GB6 B1428+4217 did not change between the long-term and the flare data sets. The measured luminosity during the flare in 2023 is poorly constrained, and does not get close to the record γ-ray luminosities measured for other high-z blazars during flaring epochs (e.g., TXS 1508+572 and PKS 0537−286, Gokus et al. 2024; Sahakyan et al. 2020, respectively).

4.2. *X-ray spectra*

Using data taken simultaneously with *Swift*-XRT and *NuSTAR*, we search for the presence of a spectral break and test for the previously reported strong soft X-ray absorption (Boller et al. 2000; Fabian et al. 2001; Worsley et al. 2004, 2006). For all modeling reported in this section, we rebin each spectrum using the optimal binning algorithm by Kaastra & Bleeker (2016).

We start by assessing the absorption in the spectra taken with contemporaneous observations in 2014 and 2023. Due to the *Swift*-XRT exposures being very short, we include all data taken within several days of the *NuSTAR* observation under the assumption that no rapid change occurs for the spectral shape or absorption. For the 2014 epoch, we include two *Swift*-XRT pointings with a combined exposure of 9.6 ks, and for the 2023 epoch, we choose seven *Swift*-XRT observations yielding a combined exposure of 18.4 ks in the soft X-ray band. We model the spectra with a `constant*tbabs*ztbabs*cflux(powerlaw)` model, in which the constant is used to counterbalance slight calibration offsets between the *NuSTAR* detectors FPMA and FPMB and *Swift*-XRT. `ztbabs` is used to account for source-intrinsic cold absorption at $z = 4.715$. We consider data taken between 0.3 and 10 keV for the XRT spectra and from 3 to 80 keV for the *NuSTAR* spectra. The resulting best fit parameters are listed in Table 4. When left as a free parameter, the neutral density ab-

Table 4. Best-fit results for an absorbed power law model (`tbabs*ztbabs*cflux(powerlaw)`) applied to two contemporaneous data sets of *NuSTAR* and *Swift*-XRT spectra taken in 2014 and 2023, respectively. $N_{\rm H}$ lists the source-intrinsic cold absorption while $N_{\rm H,Gal.}$ is fixed to the Galactic foreground value.

Date	MJD	Inst.	ObsID	Exposure [ks]	Photon Index	$\text{Flux}_{0.3-80\,\text{keV}}$ [erg cm^{-2} s^{-1}]	$N_{\rm H}$ [cm^{-2}]	χ^2/d.o.f.
2014-07-14	56852.0	N	60001103002	49.2				
2014-07-02	56840.6	S	00080752001	2.2	1.67 ± 0.04	$(5.1 \pm 0.2) \times 10^{-12}$	$(6.5^{+4.4}_{-2.9}) \times 10^{22}$	451.5 / 381
2014-07-13	56851.0	S	00080752002	7.4				
2023-12-09	60287.0	N	90901634002	58.7				
2023-12-06	60284.7	S	00016413001	3.0				
2023-12-07	60285.6	S	00016413002	2.0				
2023-12-08	60286.5	S	00016413003	2.8	$1.506 \pm +0.025$	$(1.03 \pm 0.03) \times 10^{-11}$	$(5.4^{+1.4}_{-1.2}) \times 10^{22}$	517.9 / 607
2023-12-09	60287.2	S	00016413004	2.6				
2023-12-10	60288.5	S	00016413005	2.8				
2023-12-11	60289.1	S	00016413006	2.8				
2023-12-12	60290.1	S	00016413007	2.4				

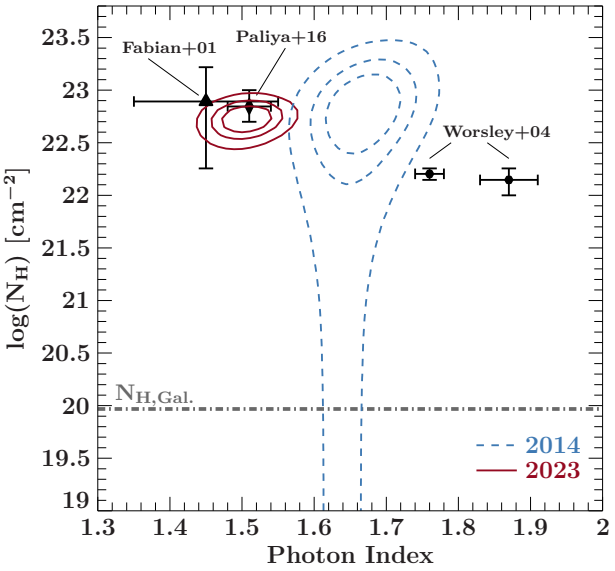

Figure 5. Confidence maps of Photon Index vs. $N_{\rm H}$ for the 2014 (*top*) and 2023 (*bottom*) datasets fit with a absorbed PL model that accounts for both the Galactic foreground absorption and an absorber at redshift $z = 4.715$.. The contours for the 2014 data are indicated by a dashed line, while the 2023 contours are shown with a solid line. From inside to outside, the lines mark the 1σ, 2σ, and 3σ contours. We include results from previous work and mark the value of the Galactic absorption column with a dash-dotted line.

sorption $N_{\rm H}$ at redshift 4.715 is found to be significantly higher than the Galactic foreground value. To investigate the correlation between $N_{\rm H}$ and the photon index, we compute confidence contours for 1σ, 2σ, and 3σ confidence for two parameters of interest that we show in Fig. 5. In the plot, we include results from previous analyses by Boller et al. (2000), Fabian et al. (2001), and Worsley et al. (2004) based on data collected in the soft X-ray range by *ROSAT*, *Beppo-SAX*, and *XMM-Newton* between 1998 and 2002. On the 2014 data, our spectral fit provides a less constraining absorbing column measurement than the analysis in Paliya et al. (2016). A scenario with no absorption beyond the Galactic column density is excluded only at 95% confidence..

Comparing the best-fit results from both epochs, the X-ray flux (as measured with an absorbed power law) is about 50% higher in 2023 than in 2014, which is likely linked to the γ-ray flare. The difference between both fluxes is on the order of $> 14\sigma$. In addition, the spectrum taken in 2023 is significantly harder while showing the same amount of absorption as the spectrum from 2014.

We further test whether other models can describe the broadband X-ray spectra equally well or better. Due to some variability present in the soft X-ray range, we now only fit strictly simultaneous data together. We test five different models: an absorbed power law with the absorption column fixed to the Galactic foreground value (PL), an absorbed power law with an additional absorption parameter at redshift $z = 4.715$ free to vary (ABS+PL), a broken power law with the absorption fixed on the Galactic value (BPL), a broken power law with the $z = 4.715$ absorption parameter being free (ABS+BPL), and a blackbody plus power law model (BB+PL). The PL model serves as our baseline, since blazars in the local Universe typically do not show a deviation from a power law with Galactic foreground absorption. We expect the results from the ABS+PL model to match the dedicated fit described in the previous paragraph, however, with slightly looser constraints given that we use only strictly simultaneous

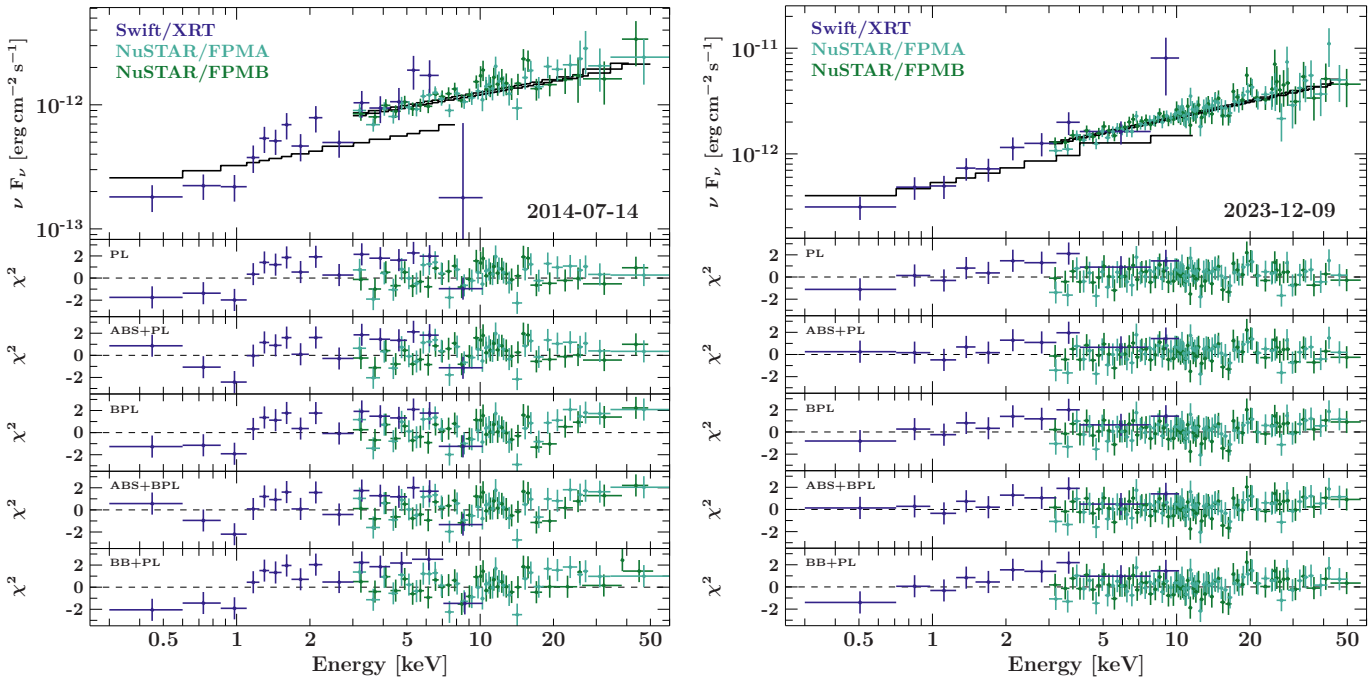

Figure 6. Broadband X-ray spectra of the observation taken in 2014 (*left*) and 2023 (*right*). In each top panel we show the spectral bins and the power law model with foreground absorption. The residual panels are shown for each model we apply and list in Table 5.

data here. The BPL model represents emission from an electron distribution with a spectral cooling break or a scenario in which two distinct processes (e.g., SSC and EC) contribute to the X-ray spectrum, with the break E_b indicating the energy where the transition occurs. ABS+BPL considers an additional intrinsic absorption on top of the broken power law. Lastly, the motivation for testing a BB+PL model originates from the predictions of bulk Comptonization of thermal photons from the BLR (Celotti et al. 2007).

The best-fit results for each model are listed in Table 5 and the spectral plots including residuals for each model are shown in Fig. 6. Based solely on the F-statistics and p-values, we find that for both epochs the BPL model yields the best fit, although for the 2014 data, the ABS+BPL model gives equally good results. The BB+PL model is an improvement compared to the PL model as well, however the fraction of the total contribution to the model by the black body compared to the power law is only on the order of 2% for both data sets. Interestingly, the ABS+PL model is an improvement compared to the PL model for the 2014 data set (p-value < 0.05), but not for the 2023 data set. However, we note that the statistics for the 2023 data already yield a satisfactory fit to the spectrum with a reduced $\chi^2 < 1$. Discriminating features between the tested spectral models appear most prominently in the soft X-ray band, covered only by *Swift*. Due to higher photon statistics and better signal to noise, the cost function (C-statistic or χ^2) in standard minimization algorithms is dominated by the *NuSTAR* data, favoring models that fit well at higher energies even if they represent a suboptimal fit of the soft X-ray spectrum. Therefore, model selection based solely on global fit statistics can be misleading.

In the following, we examine the residuals under different models (see Fig. 6) to evaluate their performance in describing the soft X-ray spectrum of GB6 B1428+4217. The 2014 data set generally shows larger residuals compared to the 2023 data set. For the latter, we find that the ABS+PL, BPL, and ABS+BPL models sufficiently describe the slope of the *Swift*-XRT data, with those models including the strong intrinsic absorption yielding better agreeing residuals at the lowest energies. For the BB+PL model, we do not see an improvement in the residuals compared to the PL model in either data set. We conclude that we cannot significantly distinguish between ABS+PL, BPL, and ABS+BPL.

When applying the broken power law model, the flux in the full 0.3–80 keV band decreases by 50% and 25% in the 2014 and 2023 epoch, respectively, but is still consistent with a significant increase by a factor of ~ 2.5 between the two epochs. While for both data sets the energy of the spectral break is consistently at ~ 20 keV, the photon index Γ_2 for the higher energies cannot be constrained for the 2014 data set (we have limited the maximum value of Γ to 4).

Paliya et al. (2016) initially presented the simultaneous *Swift*-XRT and *NuSTAR* from 2014 and reported that both a power law with additional absorption on the order of $\sim 7 \times 10^{22}\,\mathrm{cm}^{-2}$ or a broken power law with a break at $\sim$5 keV describe the data equally well, and significantly better than a power law with only Galactic foreground absorption. Our results agree with their findings with regard to the absorption strength and flux, but we obtain a softer photon index and for the broken power law model we find the break in the spectrum at much higher energies.

4.3. *X-ray variability*

Based on the 2014 and 2023 data set collected for the full X-ray band, we can confirm that the photon index as well as the flux have changed between the two epochs. In order to produce a light curve, we model each spectrum with a simple power law including Galactic foreground absorption (i.e., fixing $N_{\rm H}$), however, we exclude all data for which the exposure time is less than 0.5 ks or if the source spectrum contains less than 50 counts. In addition, observations taken within 24 hours of each other are fit simultaneously. We use C-statistics (Cash 1979) due to the low number of photons in the majority of the *Swift*-XRT spectra. The best-fit results are listed in Appendix Table 7 and the light curve is shown in Fig. 7.

Using the monitoring time ranges from 2021 May through 2021 November as well as December 2023 through February 2024, we can also study shorter term variability. In particular, as seen in Figure 7, our monitoring in 2023/2024 contains daily snapshots for the initial seven days after the γ-ray flare, followed by seven observations at four-day cadence. After a gap of 22 days, we monitored GB6 B1428+4217 with weekly cadence. We test for flux variability by fitting each light curve section to a constant flux, deriving p-values for the constant flux hypothesis using a χ^2 test. We find $p = 9.4 \times 10^{-6}$ and $p = 4.5 \times 10^{-5}$ for the 2021 and the 2023/2024 data sets, respectively, which confirms that variability is present in GB6 B1428+4217 in the 0.3–10 keV band over timescales of several days in our observer's frame, and a factor of $1/(z+1)$ shorter in the restframe of GB6 B1428+4217. To further quantify the variability time scales, we perform a standard calculation of exponential flux doubling/halving times between each flux point in each epoch, respectively. Due to the rather large uncertainties on the flux, we can only obtain one significant halving time for a flux point combination in 2023, for which we find $\tau_{\rm h} = 1.2 \pm 0.4$ days ($\sim 3.4\sigma$) in the source rest frame. Additionally, we find the most rapid and $> 2\sigma$ doubling time of 12 ± 6 hours in the 2023/2024 epoch as well.

4.4. *Optical polarization*

The optical and infrared radiation from gamma-ray emitting blazars at $z \gtrsim 3$ is generally attributed to thermal emission from the AGN accretion disk (e.g., Paliya et al. 2016, 2019; Liao et al. 2019; Marcotulli et al. 2020; Gokus et al. 2024). This interpretation is supported by two main factors: first, the high redshift shifts the disk emission, typically in the blue and ultraviolet bands in low-z AGN, towards longer wavelengths. Second, the larger estimated or inferred black hole masses in high-z blazars would result in lower temperature disks ($T_{\rm disk} \propto M_{\rm BH}^{-1/4}$, Shakura & Sunyaev 1973), further shifting the disk emission towards the optical and infrared bands.

The moderate R band polarization P = (8.6 ± 3.0)% measured from GB6 B1428+4217 indicates that this source may not conform to this scenario, at least during the gamma-ray flare examined in this study. Moderate to high levels of polarization ($3\% \lesssim P \lesssim 30\%$) are typically expected from synchrotron radiation, with higher polarization levels indicating a more ordered magnetic field in the emitting region. In contrast, thermal emission from the accretion disk is expected to be unpolarized. Combined spectral and polarization surveys of blazars converge in considering objects with $P \gtrsim 3\%$ as synchrotron-dominated (Smith et al. 2007).

To further assess whether the observed R-band polarization from GB6 B1428+4217 can distinguish between a synchrotron and thermal origin of the optical emission, we examine publicly-available optical polarization observations for other gamma-ray bright blazars (Smith 2016, [4]). We observe that objects with SEDs where optical emission is dominated by thermal disk emission or galactic foreground (Mrk 501, 3C 273, 1ES 2344+514) show optical polarizations $\leq 3\%$. Objects for which the optical SED is dominated by continuum emission from synchrotron radiation (OJ 287, 3C 279) show $P \gtrsim 10\%$. Finally, objects for which the optical emission is dominated by synchrotron continuum but show some contribution from a thermal disk component (PKS 1222+216, PKS 1510-089) show variable polarization in the range $3\% \lesssim P \lesssim 6\%$. The observed P = (8.6 ± 3.0)% in GB6 B1428+4217 suggests that the R-band emission of the quasar being dominated by synchrotron radiation from the jet, with the possibility of some contribution from thermal emission from the AGN disk.

[4] https://james.as.arizona.edu/~psmith/Fermi/

Table 5. Model comparison for the 2014 and 2023 epoch using only simultaneous data. For the BPL and the ABS+BPL models, we list the break energy E_b, and for the BB+PL model we list the peak temperature kT.

2014								
Model	N_H [cm^{-2}]	Γ_1	Γ_2	E_b / kT [keV]	Flux$_{0.3-80\,keV}$ [10^{-12} erg cm^{-2} s^{-1}]	χ^2 / d.o.f.	F-stat	p-value
PL	9.29×10^{19}	1.65 ± 0.04	–	–	5.15 ± 0.21	429.5 / 346	–	–
ABS+PL	$6.0^{+4.2}_{-2.8} \times 10^{22}$	1.67 ± 0.04	–	–	5.05 ± 0.21	422.42 / 345	5.80	0.016
BPL	9.29×10^{19}	$1.55^{+0.05}_{-0.04}$	> 3.2	$19.4^{+2.4}_{-2.3}$	3.24 ± 0.18	392.7 / 344	16.12	2.0×10^{-7}
ABS+BPL	$4.2^{+3.4}_{-2.5} \times 10^{22}$	1.59 ± 0.05	> 3.3	$20.5^{+1.9}_{-2.7}$	3.31 ± 0.17	389.04 / 343	11.90	2.0×10^{-7}
BB+PL	9.29×10^{19}	$1.74^{+0.08}_{-0.07}$	–	3.1 ± 0.5	$4.30^{+0.29}_{-0.27}$	412.72 / 344	6.99	1.05×10^{-3}
2023								
Model	N_H [cm^{-2}]	Γ_1	Γ_2	E_b / kT [keV]	Flux$_{0.3-80\,keV}$ [10^{-12} erg cm^{-2} s^{-1}]	χ^2 / d.o.f.	F-stat	p-value
PL	9.29×10^{19}	$1.500^{+0.026}_{-0.025}$	–	–	10.3 ± 0.3	275.7 / 369	–	–
ABS+PL	$3.7^{+3.8}_{-2.8} \times 10^{22}$	1.506 ± 0.026	–	–	10.3 ± 0.3	273.80 / 368	2.55	0.11
BPL	9.29×10^{19}	1.44 ± 0.04	2.21 ± 0.26	$20.3^{+1.3}_{-1.8}$	8.3 ± 0.6	261.4 / 367	10.04	5.7×10^{-5}
ABS+BPL	$2.5^{+3.6}_{-2.5} \times 10^{22}$	1.45 ± 0.04	2.20 ± 0.26	$20.4^{+1.3}_{-1.9}$	8.3 ± 0.6	260.59 / 366	7.07	1.3×10^{-4}
BB+PL	9.29×10^{19}	1.57 ± 0.06	–	$4.1^{+0.8}_{-0.9}$	9.2 ± 0.5	266.48 / 367	6.35	1.95×10^{-3}

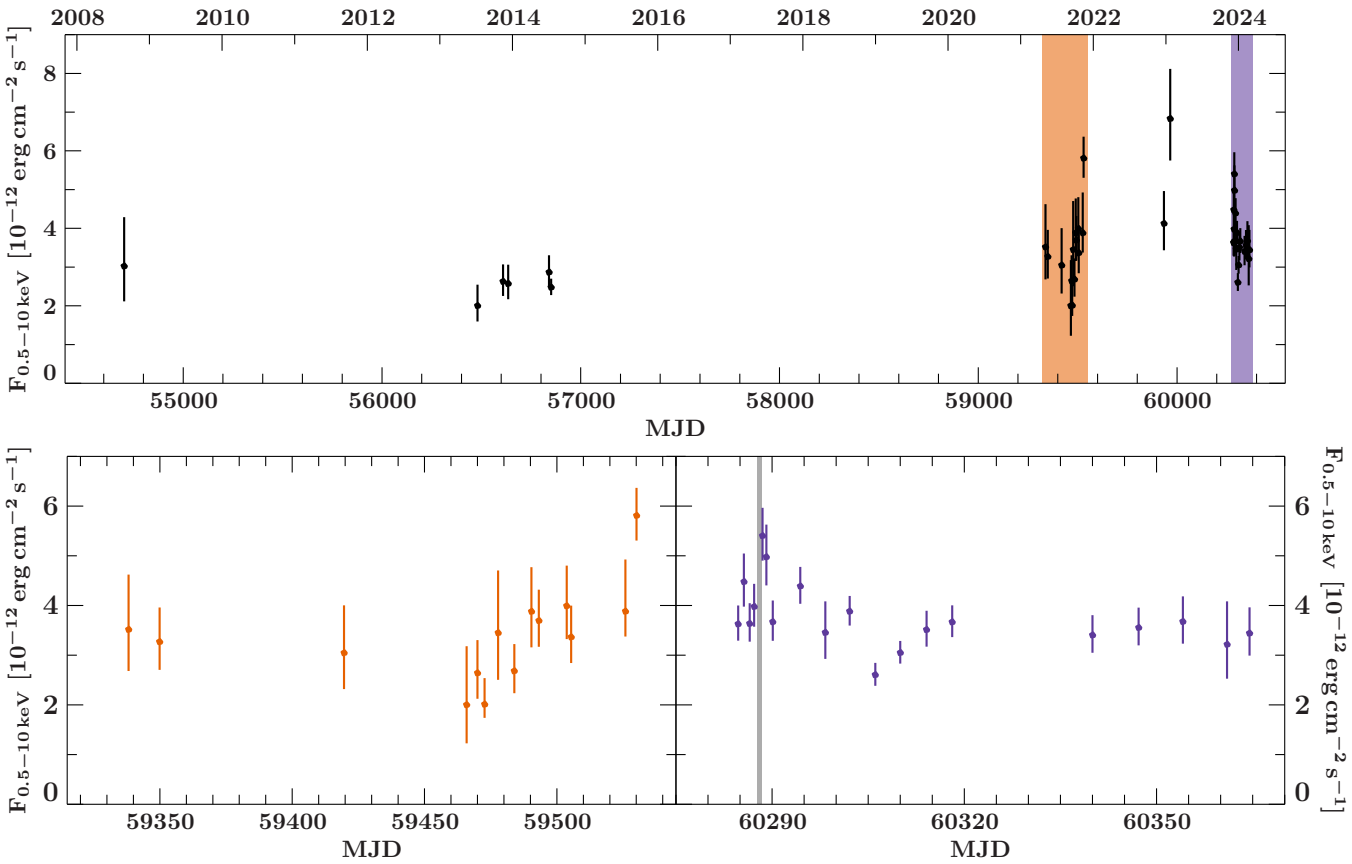

Figure 7. *Swift*-XRT light curves. Top: full LC from 2008 to 2024. Bottom: Zoom in into the denser monitoring in 2021 and 2024, where the later time range covers the time range during which the gamma-ray flare occured. The time of the *NuSTAR* DDT observation is marked by a grey shaded region in the bottom right light curve.

4.5. *Broadband SED Modeling*

We compiled quasi-simultaneous SEDs for both the low state in 2014 and the flaring state in 2023, which are shown in Fig. 8 with blue and red symbols, respectively. These data were complemented by archival radio, IR, optical, and X-ray data (black symbols). Due to the sparse simultaneous IR–optical coverage, the low-frequency component of the SED is very poorly constrained. However, the moderate polarization of $8.6 \pm 0.3\%$ during the 2024 high state suggests that jet synchrotron radiation makes a non-negligible contribution to the optical flux during that period (see §4.4). This assumption guided our choice of parameters to fit the SEDs, using the stationary, single-zone leptonic model developed by Böttcher et al. (2013).

The Böttcher et al. (2013) leptonic model assumes a spherical emission region of radius R_b propagating along the jet with bulk Lorentz factor Γ. It is magnetized with a magnetic field of strength B. A non-thermal, relativistic electron population is injected by an unspecified rapid acceleration mechanism, with spectral index q and low- and high-energy cut-offs at $\gamma_{\rm min}$ and $\gamma_{\rm max}$, respectively. The code then evaluates an equilibrium distribution resulting from the balance between injection, radiative cooling, and escape from the emission region on an energy-independent escape time scale $t_{\rm esc} = \eta_{\rm esc}\, R_b/c$. Radiation mechanisms included in the code are synchrotron radiation, synchrotron-self-Compton (SSC), and external-Compton (EC) from scattering of the direct accretion-disk radiation, EC (disk) and an isotropic (in the AGN rest frame) thermal radiation field, in this case with parameters appropriate for IR emission from the dust torus, EC (DT). We use this model to perform a fit-by-eye and obtained acceptable fits using the parameters listed in Table 6. Guided by the hardening of the *Fermi*-LAT spectrum from 2014 to 2023, the most significant parameter changes between the two states is a significantly harder electron injection spectrum, extending to much higher energies during the flaring state. Note, however, that the SED, especially the low-frequency component, is poorly constrained, resulting in significant parameter degeneracies. Therefore, the values listed in Table 6 should be considered as constituting a plausible, but not unique, scenario that can describe the SED in the framework of a single-zone leptonic emission model. For example, we note that the EC (DT) component is subdominant, with the high-energy radiation being largely described by EC (disk) and SSC emission. Other radiation fields, such as the BLR, could also contribute to the observed γ-ray radiative output. As is commonly found in blazars, the high-energy emission region modeled here is optically thick to synchrotron self-absorption in the radio band. Therefore, the radio emission is expected to be produced in the larger-scale jet, not modeled here.

Table 6. SED model fit parameters used for the fits shown in Fig. 8. q = electron spectral index at injection. d = injection height.

Parameter	Long-term	Flare
L_e [erg s^{-1}]	4.7×10^{45}	5.7×10^{45}
$\gamma_{\rm min}$	100	60
$\gamma_{\rm max}$	2.5×10^3	1×10^5
q	2.9	2.5
B [G]	8.0	7.0
$\eta_{\rm esc}$	10	10
d [pc]	0.12	0.1
Γ	14.6	14.6
$L_{\rm disk}$ [erg s^{-1}]	2×10^{47}	2×10^{47}
R_b [cm]	8×10^{15}	8×10^{15}
$M_{\rm BH}$	1.7×10^9	1.7×10^9
$T_{\rm DT}$ [K]	1000	1000
$u_{\rm DT}$ [erg cm^{-3}]	6.0×10^{-4}	6.0×10^{-4}
L_B [erg s^{-1}]	3.3×10^{45}	2.5×10^{45}
ϵ_{Be}	0.691	0.435

5. DISCUSSION

5.1. *Broadband emission*

We made use of existing measurements of some properties of GB6 B1428+4217 as starting points to derive our SED model parameters. The reported mass estimates for this source range from $\sim 1.7 \times 10^9\, M_\odot$ to $\sim 7.4 \times 10^9\, M_\odot$ (e.g., Shen et al. 2011; Diana et al. 2022), where the former is derived from the dispersion of the C IV line, and the latter is obtained through measuring the full width half maximum of said emission line. We find that the expected accretion disk emission from a $1.7 \times 10^9\, {\rm M}_\odot$ black hole, in agreement with values reported in the literature, can describe the observed optical to infrared SED. Our choice of the bulk Lorentz factor, $\Gamma = 14.6$, was motivated by a 22-year long radio campaign using very-large baseline interferometry (Zhang et al. 2020). Our polarization measurement in the optical R band helps us to determine how much of the emission in this band can be attributed to synchrotron emission, since the measured polarization of 8.6% is incompatible with a pure accretion-disk spectrum. As a result, our assumption of the amount of synchrotron emission also led to our choice for the magnetic field strength and to achieve equipartition between the B-field and the relativistic leptons.

Some studies have modeled the broadband SED of GB6 B1428+4217 in the past. Ghisellini & Tavec-

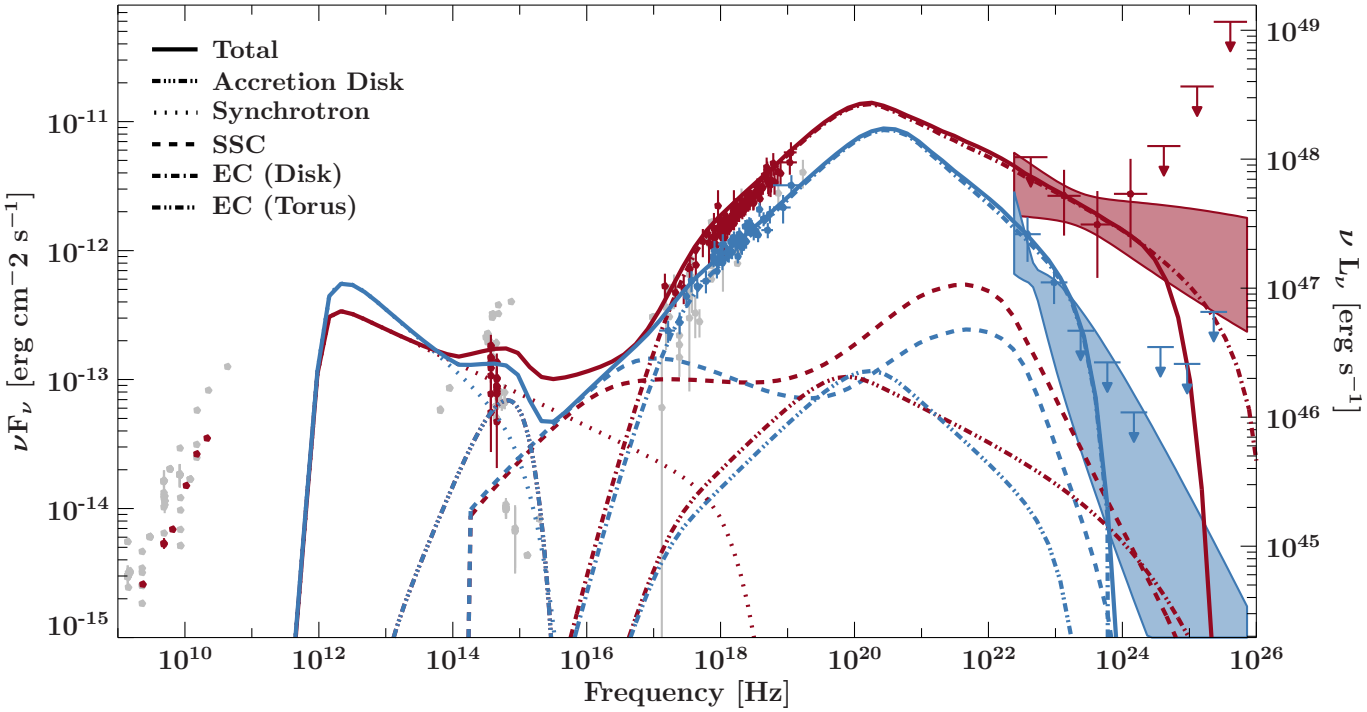

Figure 8. Broadband SED of GB6 B1428+4217 for non-simultaneous, archival multiwavelength data (blue), and for the active state in 2023 with contemporaneous data (red), modeled with the stationary one-zone leptonic model described in Böttcher et al. (2013).

chio (2009) used a leptonic model with a variable distance of the dissipation region for the different states of the source based on X-ray data collected with *Beppo-SAX*, *ASCA*, and *XMM-Newton*. They find that the dissipation region lies within the BLR at about 1500 Schwarzschild radii, R_S, from the central SMBH. For both states that we model with more recent X-ray data and including γ-ray data from LAT, we find that the dissipation region lies even closer to the SMBH, at $\sim 740\,R_S$ during the long-term average state, and at $\sim 610\,R_S$ during the flaring event in 2023. Using the same model as Ghisellini & Tavecchio (2009), but using a newer X-ray data set from 2014, Paliya et al. (2016) modeled broadband data similar to our long-term SED. While we use similar values for the black hole mass, the bulk Lorentz factor, and the accretion disk luminosity, the major difference between both models is that Paliya et al. (2016) describe a magnetically dominated jet while we model GB6 B1428+4217 under the assumption of equipartion. Comparing the properties of the class of high-z redshift blazars to our results from the SED modeling, we find that some parameters derived for GB6 B1428+4217 seem to lie at the higher end of the range reported by (Paliya et al. 2020), in particular the accretion disk luminosity, the bulk Lorentz factor, and the magnetic field strength. The long-term average γ-ray luminosity and photon index of GB6 B1428+4217

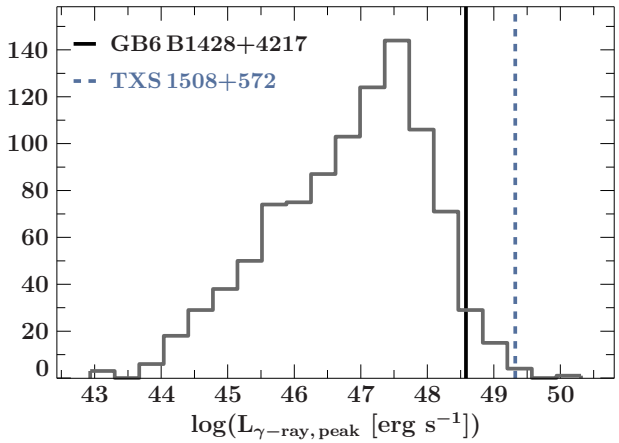

Figure 9. Distribution of peak γ-ray luminosities obtained from the 4FGL-DR4 with redshift information taken from 4LAC-DR3. The histogram is computed for a number of 20 bins between the minimum and maximum luminosities with equal spacing in the logarithmic space. We mark the peak γ-ray luminosities for GB6 B1428+4217 and TXS 1508+572 (see Gokus et al. 2024) with solid and dashed lines, respectively.

are in very good agreement with the values found for other γ-ray detected blazars at $z > 3$ (Ackermann et al. 2017).

5.2. *Comparison with other luminous blazars*

To put the luminosity of the γ-ray flare from GB6 B1428+4217 in context, we use the peak yearly fluxes and time-averaged γ-ray photon indices from the *Fermi* 4FGL-DR4 catalog (Ballet et al. 2023) with redshift estimates from 4LAC-DR3 (Ajello et al. 2022) to calculate k-corrected peak luminosities for a sample of of 977 γ-ray detected blazars. These peak luminosities may be underestimated compared to shorter timescale γ-ray flares reported in the literature. The resulting peak luminosity distribution is shown in Fig. 9. The flare luminosity of GB6 B1428+4217 of $(3.9 \pm 3.8) \times 10^{48}\,\mathrm{erg\,s^{-1}}$ puts it in the top 5% of most luminous flares seen by *Fermi*.

The dimensionless Compton Dominance (CD) parameter, defined as the ratio between the peak synchrotron luminosity, $L_{\rm syn}$, and the peak IC luminosity, $L_{\rm IC}$, can be used as a proxy for the relative energy densities of external radiation and magnetic fields (e.g., Pacciani et al. 2014):

$$CD = \frac{L_C}{L_{\rm syn}} = \frac{U'_{\rm ext}}{U'_B} = \frac{U_{\rm ext}\Gamma^2_{\rm bulk}}{U'_B} \qquad (1)$$

Based on the peak values of the low- and high-energy component listed in the 4LAC-DR3 (Ajello et al. 2022), we compute CD values based on the average SED for a large sample of blazars. GB6 B1428+4217 displays a high Compton dominance of $CD \sim 15$ in an average SED state, increasing to $CD \sim 40$ during the 2023 γ-ray flare.

We find five sources in the same peak luminosity bin as GB6 B1428+4217 that have been studied in detail in the literature: PKS 0346−27, PKS 0402−362, PKS 0528+134, TXS 0536+145 and PKS 2023−07, with redshifts in the range $0.99 \leq z \leq 2.69$. GB6 B1428+4217 is most similar to PKS 0346−27, which shows a high $CD \sim 25$ in its average SED state (Angioni et al. 2019; Kamaram et al. 2023), increasing to ~ 45 during flares (Angioni et al. 2019)[5]. The other four objects show a smaller Compton dominance, with their time-averaged SEDs yielding $CD \lesssim 5$.

5.3. *High-redshift blazars within the blazar population*

For a comparison with the entire blazar class, we use the 4LAC-DR3 and plot the average Compton dominance as a function of redshift of the 4LAC blazars for which a redshift is known in Fig. 10. At higher redshifts, we are biased toward detections of more luminous sources due to the limited sensitivity of *Fermi*-LAT, hence we are likely missing detections of blazars with

[5] We note that the Compton dominance is not explicitly listed in other publications. Hence, we calculate these values from reading the peak fluxes of the SED figures.

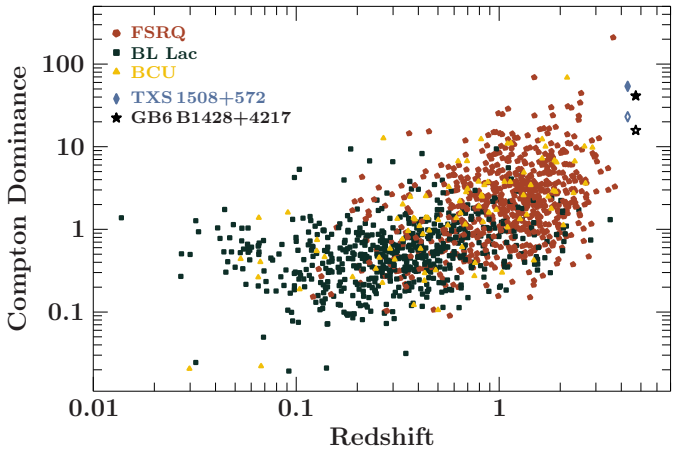

Figure 10. Compton dominance over redshift for blazars with a known redshift and Compton peak listed in the 4LAC-DR3 (Ajello et al. 2022). We include the Compton dominance of TXS 1508+572 (diamond symbol) and GB6 B1428+4217 (star symbol) for both the quiet (empty symbol) and active (filled symbols) states to illustrate the significant change during flaring episodes.

a small Compton dominance in the early Universe. 53 blazars and blazar-like AGN exhibit a strong Compton dominance ($CD \geq 10$), with a median redshift $z = 1.55$ for these sources. Only ten sources at $z < 1$ (i.e., within the last ~ 6 billion years) belong to this group, while 15 fall into the time of cosmic noon ($z > 2$).

We add GB6 B1428+4217 and TXS 1508+572 (Gokus et al. 2024) to Fig. 10 with distinct symbols showing their Compton dominance during quiet-state/average SED (unfilled symbols) and flaring states (filled symbols). Both objects show an increase in CD during flares. The increase of the Compton dominance by a significant factor has also been observed for luminous flares in FSRQ with $z < 1$, e.g., 3C 279 (Hayashida et al. 2015), or 3C 454.3 (Zhou et al. 2021), as well as for much less luminous, but blazar-like sources such as γ-loud Narrow Line Seyfert 1 galaxies (e.g., PKS 2004−447; Gokus et al. 2021). However, on average, most blazars exhibit a low Compton dominance: based on values derived from the 4LAC-DR3, the average CD for BL Lac objects is 0.9, while it is 3.9 for FSRQs.

Nalewajko & Gupta (2017) discuss in detail that the denser external radiation fields that are responsible for the external IC emission can result from a more luminous accretion disk, indicating that Compton dominance can be used as a proxy for more efficient accretion processes of the central SMBH. Furthermore, they find that Compton dominance scales with the equipartition parameter $\epsilon_{Be} = P_B/P_e$, which for values < 1 indicates that the jet is likely matter-dominated. For GB6 B1428+4217, $0.4 < \epsilon_{Be} < 0.7$, within that range.

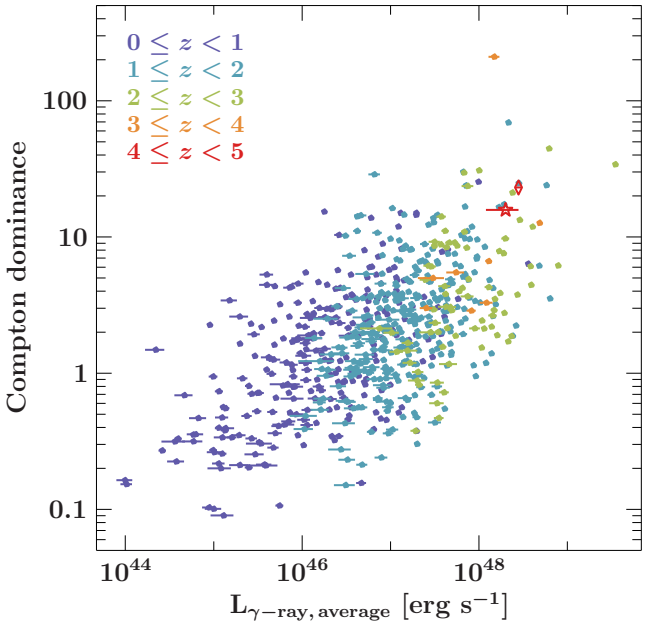

Figure 11. Compton dominance vs. average γ-ray luminosity for all FSRQs with a known redshift and Compton peak listed in the 4LAC-DR3 (Ajello et al. 2022). TXS 1508+572 (diamond symbol) and GB6 B1428+4217 (star symbol), for which we also show the average γ-ray luminosities and Compton dominance values, are the only two blazars with $z > 4$.

In addition, a correlation between the Eddington ratio and the Compton dominance has been reported by Paliya et al. (2021).

The detection of FSRQ at high redshifts allows us to verify the predictions of the blazar sequence (Fossati et al. 1998; Meyer et al. 2011) at the highest luminosities. The blazar sequence describes how more luminous blazars tend to have lower synchrotron peak frequencies and higher Compton dominance, driven by stronger radiative cooling via external photon fields. Originally built on a radio and X-ray selected sample, the γ-ray selected *Fermi* blazar sequence (Ghisellini et al. 2017) revealed that the shift of the peak frequencies is only seen for BL Lac-type objects, while the increasing γ-ray luminosity (and with it an increased Compton dominance) is solely present for FSRQs. Other work even questions the validity of the blazar sequence altogether, and it has been argued that the correlation of the peak frequency and peak luminosity is an observational selection effect (e.g., Nieppola et al. 2008; Giommi et al. 2012; Fan et al. 2017; Keenan et al. 2021). A detailed review on this topic is given by Prandini & Ghisellini (2022). In the framework of the sequence, very luminous FSRQs have high accretion rates, producing dense external radiation fields (e.g., from the broad line region) that enhance Compton scattering and explain their observed high Compton dominance. Figure 11 shows this correlation for a large sample of detected FSRQ, with values calculated from extracted average fluxes and redshifts from the 4FGL-DR4 and 4LAC-DR3 catalogs.

Due to the increasing sampling volume, the median luminosity of FSRQs is observed to increase with increasing redshift. At $z > 4$, TXS 1508+572 and GB6 B1428+4217 show Compton dominance values of 23 and 16, respectively. While these are among the highest values in the FSRQ sample, they are not outliers but follow the general trend of rising Compton dominance with increasing luminosity observed also at lower redshifts. Based on the observed trend, we can infer that gamma-ray detected blazars at high redshift are compatible with being objects with high accretion rates, as expected from the blazar sequence. With higher accretion rates, there is greater available accretion power, resulting in more powerful jets. Additionally, the accretion disk becomes brighter and more radiatively efficient, capable of ionizing surrounding gas such as the broad line region. These dense external photon fields serve as seed photons for Compton scattering, enhancing the radiative cooling rate of the non-thermal electrons in the jet. This process leads to a higher observed Compton dominance.

Given that the energy density of the cosmic microwave background (CMB) scales as $(1 + z)^4$, one might expect Compton scattering on the CMB to significantly contribute to the γ-ray SED for high-redshift objects. However, the modeling of SEDs and the absence of an excess in Compton dominance for high-redshift objects do not suggest that Compton scattering on the CMB is a significant cooling mechanism. This implies that the dissipation region of the blazar must be located within $< 10^6$ gravitational radii from the central black hole, where the infrared dust torus and the broad line region dominate the radiation energy density in the jet environment (Ghisellini & Tavecchio 2009).

In optical surveys, the number density of quasars is highest at $z \sim$ 2-3 (Richards et al. 2006), at the peak epoch of black hole accretion and star formation in the Universe. Our analysis shows that energy dissipation in γ-ray-emitting FSRQs at $z > 4$ seems to follow the same mechanisms observed in luminous FSRQs found in our local universe ($z < 1$).

5.4. *Interpretation of anomalous X-ray spectrum*

We confirm the presence of a peculiar feature in the broadband X-ray spectrum of GB6 B1428+4217 in data obtained during a flaring state of the source.

In earlier data, such as the 1999 *BeppoSAX* spectra reported by Fabian et al. (2001), a warm absorber with an equivalent column density of $n_{\rm H} \sim 3 \times 10^{22}$ cm^{-2} was

suggested to explain the flattening of the X-ray spectrum towards low energies–compared to the higher energy power-law (Boller et al. 2000; Fabian et al. 2001; Worsley et al. 2004, 2006). The expectation under this scenario is that the column density of this local warm absorber does not change significantly over time and similar column densities are measured throughout time. In particular, at a higher overall X-ray flux, the presence of a warm absorber would likely be seen at higher significance as a result of increased statistics. Our analysis of the 2023 X-ray spectra does support this scenario, but we also find that a broken power law (without a need for intrinsic absorption) statistically does describe our X-ray data equally well. Additionally, a high intrinsic absorption would lead to large reddening in the optical band, which is not observed (Paliya et al. 2016).

Celotti et al. (2007) proposed an alternative interpretation of the anomalous soft X-ray spectrum of GB6 B1428+4217, suggesting that the flattening toward low energies could be due to a bulk Compton component. First proposed in Begelman & Sikora (1987), the bulk Compton process involves cold, thermal electrons in the jet cooling on radiation fields such as disk or BLR emission via Compton scattering, resulting in a soft X-ray excess. In this scenario, the spectrum is expected to flatten at soft X-ray energies due to the presence of an additional black body component (bulk Compton) peaking at mid X-ray temperatures (Celotti et al. 2007). As described in Section 4.2, we are able to fit the combined *Swift* and *NuSTAR* spectra from 2014 and 2023 with a black body peaking at $kT \sim 3 - 4\,\mathrm{keV}$, but the ratio of black body to power law flux is very low, and the residuals do not indicate that the additional black body component significantly improves the spectral fit.

The limited photon statistics in the soft X-ray band from *Swift* prevent a high-confidence assessment of features such as local cold absorption or a bulk Compton component. Definitive tests for these scenarios will require high-fidelity soft X-ray spectra (e.g., from *XMM-Newton*) obtained at different flux states. A bulk Compton feature would be more pronounced at lower levels of external Compton continuum, while absorption by local cold gas would imprint similar spectral signatures regardless of flux level. Simultaneous *NuSTAR* observations would help constrain the hard X-ray component, improving the sensitivity to resolve anomalous soft X-ray features.

6. SUMMARY AND CONCLUSION

In this work, we have analyzed the high-energy flare from what is currently the most distant γ-ray blazar GB6 B1428+4217 detected by *Fermi*-LAT. At X-ray energies, our follow-up campaign consisted of a *NuSTAR* observation during the flaring epoch, as well as 19 observations with *Swift*, with which we monitored the source for over two months. Optical data in the R and I bands were obtained with telescopes at the Sierra Nevada Observatory and the Perkins telescope. Using the latter, we measured an optical polarization of $\sim 8\%$, which confirms that the optical emission during the flare was dominated by synchrotron emission and puts constraints on the luminosity of the accretion disk, which is otherwise poorly constrained for this source. The flare was accompanied by harder-when-brighter behavior at γ-ray energies, as is common in FSRQs. The γ-ray luminosity of GB6 B1428+4217 during the flare places it amongst the top 5% of luminous flaring events recorded by the *Fermi* observatory. Past X-ray observations of the blazar have revealed peculiar spectral features below 2 keV, which have been interpreted to be caused by different absorption scenarios as well as bulk Comptonization of thermal photons. In the combined fit of the *Swift*-XRT and *NuSTAR* spectra obtained during the flaring event, we also find evidence for these features. However, we are not able to conclusively rule out whether these originate from source-intrinsic absorption or a change or transition in the X-ray spectrum.

The hard X-ray flux of GB6 B1428+4217 showed a significant increase during the flare, and the *NuSTAR* observation provided essential data to model the high-energy emission, which we attribute to external Compton emission connected to the accretion disk.

This high-z blazar presents itself as a prototypical MeV blazar with its high-energy component peaking at $\sim 1\,\mathrm{MeV}$ in the broadband SED. The high Compton dominance presented in its SED fits into the correlation of γ-ray luminosity with Compton dominance of FSRQs. Despite the high observed luminosity of $\sim 4 \times 10^{48}\,\mathrm{erg\,s^{-1}}$ and a Compton dominance of 41, the observed SED, when put in context of the larger FSRQ population, suggests that the particle acceleration and cooling mechanisms at play at $z = 4.71$ are the same as observed in local high-power FSRQs.

Flaring events from more than 12 billion years ago can enable us to study early blazars at γ-ray energies. If blazars show a significant increase in Compton dominance during a flare (such as GB6 B1428+4217 or TXS 1508+572), the chance for detectability with the upcoming Compton Spectrometer and Imager (COSI; Tomsick et al. 2019, 2024) may increase the currently predicted number of four $z > 3$ blazar detections (Marcotulli et al. 2022). Based on the average flaring event occurrence among the sample of our ~ 80 high-z blazars,

which is one every 14 months, COSI might be able to detect one or two additional sources.

A. G. acknowledges funding by NASA through grant 80NSSC24K0813 and the McDonnell Center for the Space Sciences at Washington University in Saint Louis. A. G. and M. E. thank Jules Halpern for his evaluation on the different redshift measurements. The authors thank the *NuSTAR* team for granting the DDT observation of GB6 B1428+4217 in December 2023. The IAA team acknowledges financial support through the Severo Ochoa grant CEX2021-001131-S funded by MCIN/AEI/10.13039/501100011033 and through grants PID2019-107847RB-C44 and PID2022-139117NB-C44. J.O.-S. and D.M. acknowledge financial support from the project ref. AST22_00001_9 with founding from the European Union - NextGenerationEU, the *Ministerio de Ciencia, Innovación y Universidades, Plan de Recuperación, Transformación y Resiliencia*, the *Consejería de Universidad, Investigación e Innovación* from the *Junta de Andalucía* and the *Consejo Superior de Investigaciones Científicas*. J.O.-S. also acknowledges founding from INFN Cap. U.1.01.01.01.009. The research at Boston University was supported in part by the National Science Foundation grant AST-2108622, and NASA Fermi Guest Investigator grant 80NSSC23K1507. This study was based in part on observations conducted using the 1.8m Perkins Telescope Observatory (PTO) in Arizona, which is owned and operated by Boston University. This research made use of hips2fits,[6] a service provided by CDS. In this work, the author made use of a collection of ISIS functions (ISIS scripts) provided by ECAP/Remeis observatory and MIT (https://www.sternwarte.uni-erlangen.de/isis/). Partly based on observations with the 100-m telescope of the MPIfR (Max-Planck-Institut für Radioastronomie) at Effelsberg. FE, JH, and MK, acknowledge support from the Deutsche Forschungsgemeinschaft (DFG, grants 447572188, 465409577). JW acknowledges funding through DFG Research Unit (Forschungsgruppe) FOR 5195 – Relativistic Jets In Active Galaxies.

Facilities: *Fermi*-LAT, *Swift*-XRT, *NuSTAR*, Perkins, Sierra Nevada, Effelsberg

Software: ISIS, HEASOFT

APPENDIX

A. BEST-FIT VALUES FROM X-RAY ANALYSIS

In Table 7, we list all analyzed *Swift*-XRT observations and best fit results that have been plotted in the light curve shown in Fig. 7.

Table 7. Best fit results from *Swift*-XRT fits with `tbabs*ztbabs*pegpwrlw`, with fixed absorption ($N_{\rm H,Gal.} = 9.29 \times 10^{19}\,{\rm cm}^{-2}$ and $N_{\rm H,z} = 6.0 \times 10^{22}\,{\rm cm}^{-2}$).

MJD	ObsID	Counts	Exposure [ks]	$\rm Flux_{0.3-10\,keV}$ $[10^{-12}\,{\rm erg\,cm^{-2}\,s^{-1}}]$	Photon Index	Cash Statistics	Exp. C value + var
54702.9	00036798001	26	0.5	$3.0^{+1.3}_{-1.0}$	0.9 ± 0.4	25.89	17.39±5.17
56480.8	00036798002	40	1.1	$2.0^{+0.6}_{-0.5}$	$1.32^{+0.26}_{-0.27}$	28.64	38.42±7.13
56609.1	00036798006	74	1.4	$2.6^{+0.5}_{-0.4}$	1.59 ± 0.20	78.64	61.42±9.39
56634.9	00036798007	61	1.2	2.6 ± 0.5	$1.58^{+0.22}_{-0.21}$	68.89	52.94±8.63
56840.6	00080752001	104	2.2	$2.9^{+0.5}_{-0.4}$	1.30 ± 0.17	69.04	97.69±11.26
56851.0	00080752002	295	7.4	$2.48^{+0.23}_{-0.21}$	1.31 ± 0.10	187.85	227.60±17.89
59337.2	03110986004	8	0.3				
59338.2	03110986005	20	0.3	$3.5^{+1.2}_{-0.9}$	1.2 ± 0.4	53.72	34.01±7.05
59339.2	03110986012	18	0.1				
59349.9	03111053001	49	0.9	$3.3^{+0.7}_{-0.6}$	1.54 ± 0.23	40.88	46.21±8.08
59419.6	03111053003	36	0.7	$3.0^{+1.0}_{-0.8}$	1.0 ± 0.4	25.15	33.15±6.45
59465.9	03111053004	16	0.5	$2.0^{+1.2}_{-0.8}$	0.8 ± 0.5	6.41	16.06±4.69
59470.0	03111053006	36	0.8	$2.6^{+0.7}_{-0.6}$	1.52 ± 0.27	29.49	34.42±6.70
59472.7	03111053007	68	1.9	$2.01^{+0.53}_{-0.28}$	$1.45^{+0.20}_{-0.26}$	41.78	61.85±9.11
59477.8	03111053008	27	0.8	$3.5^{+1.3}_{-1.0}$	0.7 ± 0.4	24.56	25.57±5.80
59483.9	03111053009	63	1.4	$2.7^{+0.6}_{-0.5}$	$1.40^{+0.22}_{-0.21}$	46.98	57.88±8.82
59490.4	03111053012	53	0.9	$3.9^{+0.9}_{-0.8}$	1.17 ± 0.23	33.04	50.40±8.12
59493.2	03111053013	84	1.3	$3.7^{+0.7}_{-0.6}$	$1.41^{+0.19}_{-0.18}$	72.75	70.03±9.72
59503.7	03111053014	65	1.2	$4.0^{+0.9}_{-0.7}$	1.13 ± 0.21	74.37	54.64±8.97
59505.4	03111053015	67	1.1	$3.4^{+0.7}_{-0.6}$	1.47 ± 0.21	63.11	57.64±8.53
59525.9	03111053017	55	0.7	$3.9^{+1.1}_{-0.6}$	$1.55^{+0.20}_{-0.26}$	71.82	50.58±8.15
59530.0	03111053018	84	0.8	5.8 ± 0.6	1.50 ± 0.11	176.01	187.92±15.47
59530.2	03111053019	132	1.3				
59934.4	00080752003	62	0.9	$4.1^{+0.9}_{-0.7}$	1.32 ± 0.21	48.14	58.95±8.77
59965.8	00080752004	72	1.1	$6.8^{+1.3}_{-1.1}$	1.20 ± 0.20	57.02	67.23±9.38
60284.7	00016413001	199	3.0	3.6 ± 0.4	1.50 ± 0.12	118.90	168.55±15.04
60285.6	00016413002	139	2.0	4.5 ± 0.6	1.31 ± 0.14	100.24	120.22±12.84
60286.5	00016413003	175	2.8	$3.6^{+0.5}_{-0.4}$	1.38 ± 0.13	154.01	146.31±14.04
60287.2	00016413004	174	2.6	4.0 ± 0.5	1.31 ± 0.13	134.68	150.08±14.13
60288.5	00016413005	202	2.8	5.4 ± 0.6	1.46 ± 0.12	126.58	167.32±15.28
60289.1	00016413006	156	2.8	$5.0^{+0.7}_{-0.6}$	1.08 ± 0.14	103.74	141.20±13.64
60290.1	00016413007	156	2.4	$3.7^{+0.5}_{-0.4}$	1.42 ± 0.13	98.43	135.02±13.44
60294.4	00016413008	294	4.9	4.4 ± 0.4	1.29 ± 0.10	168.90	229.57±18.13
60298.3	00016413009	84	2.0	$3.5^{+0.7}_{-0.6}$	$0.96^{+0.18}_{-0.19}$	72.38	76.15±10.19
60302.1	00016413010	353	5.6	$3.88^{+0.31}_{-0.29}$	1.24 ± 0.09	215.48	258.94±19.59
60306.1	00016413011	235	5.3	$2.60^{+0.25}_{-0.22}$	1.50 ± 0.11	143.20	181.87±16.22
60310.0	00016413012	342	6.3	$3.05^{+0.24}_{-0.22}$	1.46 ± 0.09	155.48	242.16±19.29
60314.1	00016413013	200	3.5	3.5 ± 0.4	1.28 ± 0.12	134.41	157.03±14.80
60318.1	00016413014	280	5.5	3.7 ± 0.4	1.22 ± 0.10	192.59	214.93±17.34
60340.0	00016413015	153	2.7	$3.4^{+0.5}_{-0.4}$	1.41 ± 0.13	112.10	125.51±13.01
60347.2	00016413016	172	3.3	$3.6^{+0.5}_{-0.4}$	1.40 ± 0.13	96.82	152.99±14.29
60354.1	00016413017	131	2.9	$3.7^{+0.6}_{-0.5}$	1.14 ± 0.15	89.53	123.92±12.79
60361.0	00016413018	40	1.0	$3.2^{+0.9}_{-0.7}$	1.06 ± 0.26	49.92	35.36±7.07
60364.5	00016413019	111	2.3	$3.4^{+0.6}_{-0.5}$	1.15 ± 0.16	107.70	99.21±11.58

REFERENCES

Abdo, A. A., Ackermann, M., Ajello, M., et al. 2010, ApJS, 188, 405, doi: 10.1088/0067-0049/188/2/405

Abdollahi, S., Acero, F., Ackermann, M., et al. 2020, ApJS, 247, 33, doi: 10.3847/1538-4365/ab6bcb

Ackermann, M., Ajello, M., Baldini, L., et al. 2017, ApJL, 837, L5, doi: 10.3847/2041-8213/aa5fff

Agudo, I., Molina, S., Gómez, J. L., et al. 2012, International Journal of Modern Physics: Conference Series, 08, 299, doi: 10.1142/S2010194512004746

Ajello, M., Baldini, L., Ballet, J., et al. 2022, ApJS, 263, 24, doi: 10.3847/1538-4365/ac9523

Angioni, R., Nesci, R., Finke, J. D., Buson, S., & Ciprini, S. 2019, A&A, 627, A140, doi: 10.1051/0004-6361/201935461

Bañados, E., Momjian, E., Connor, T., et al. 2024, Nature Astronomy, doi: 10.1038/s41550-024-02431-4

Ballet, J., Bruel, P., Burnett, T. H., Lott, B., & The Fermi-LAT collaboration. 2023, arXiv e-prints, arXiv:2307.12546, doi: 10.48550/arXiv.2307.12546

Begelman, M. C., & Sikora, M. 1987, ApJ, 322, 650, doi: 10.1086/165760

Begelman, M. C., Volonteri, M., & Rees, M. J. 2006, MNRAS, 370, 289, doi: 10.1111/j.1365-2966.2006.10467.x

Belladitta, S., Moretti, A., Caccianiga, A., et al. 2020, A&A, 635, L7, doi: 10.1051/0004-6361/201937395

Benke, P., Gokus, A., Lisakov, M., et al. 2024, A&A, 689, A43, doi: 10.1051/0004-6361/202450153

Bogdán, Á., Goulding, A. D., Natarajan, P., et al. 2024, Nature Astronomy, 8, 126, doi: 10.1038/s41550-023-02111-9

Boller, T., Fabian, A. C., Brandt, W. N., & Freyberg, M. J. 2000, MNRAS, 315, L23, doi: 10.1046/j.1365-8711.2000.03635.x

Böttcher, M., Reimer, A., Sweeney, K., & Prakash, A. 2013, ApJ, 768, 54, doi: 10.1088/0004-637X/768/1/54

Bromm, V., & Loeb, A. 2003, ApJ, 596, 34, doi: 10.1086/377529

Burke, C. J., Liu, X., & Shen, Y. 2024, MNRAS, 527, 5356, doi: 10.1093/mnras/stad3592

Cammelli, V., Monaco, P., Tan, J. C., et al. 2025, MNRAS, 536, 851, doi: 10.1093/mnras/stae2663

Cash, W. 1979, ApJ, 228, 939, doi: 10.1086/156922

Celotti, A., Ghisellini, G., & Fabian, A. C. 2007, MNRAS, 375, 417, doi: 10.1111/j.1365-2966.2006.11289.x

Cheung, C. C., Stawarz, Ł., Siemiginowska, A., et al. 2012, ApJL, 756, L20, doi: 10.1088/2041-8205/756/1/L20

Diana, A., Caccianiga, A., Ighina, L., et al. 2022, MNRAS, 511, 5436, doi: 10.1093/mnras/stac364

Domínguez, A., Østergaard Kirkeberg, P., Wojtak, R., et al. 2024, MNRAS, 527, 4632, doi: 10.1093/mnras/stad3425

Eppel, F., Kadler, M., Heßdörfer, J., et al. 2024, A&A, 684, A11, doi: 10.1051/0004-6361/202348262

Escudero Pedrosa, J., Morcuende Parrilla, D., & Otero-Santos, J. 2024a, IOP4, v1.4.1, Zenodo, doi: 10.5281/zenodo.10222722

Escudero Pedrosa, J., Agudo, I., Morcuende, D., et al. 2024b, AJ, 168, 84, doi: 10.3847/1538-3881/ad5a80

Fabian, A. C., Brandt, W. N., McMahon, R. G., & Hook, I. M. 1997, MNRAS, 291, L5, doi: 10.1093/mnras/291.1.L5

Fabian, A. C., Celotti, A., Iwasawa, K., & Ghisellini, G. 2001, MNRAS, 324, 628, doi: 10.1046/j.1365-8711.2001.04348.x

Fabian, A. C., Celotti, A., Pooley, G., et al. 1999, MNRAS, 308, L6, doi: 10.1046/j.1365-8711.1999.02910.x

Fabian, A. C., Iwasawa, K., McMahon, R. G., et al. 1998, MNRAS, 295, L25, doi: 10.1046/j.1365-8711.1998.29511483.x

Fan, J. H., Yang, J. H., Xiao, H. B., et al. 2017, ApJL, 835, L38, doi: 10.3847/2041-8213/835/2/L38

Fossati, G., Maraschi, L., Celotti, A., Comastri, A., & Ghisellini, G. 1998, MNRAS, 299, 433, doi: 10.1046/j.1365-8711.1998.01828.x

Ghisellini, G., Haardt, F., Della Ceca, R., Volonteri, M., & Sbarrato, T. 2013, MNRAS, 432, 2818, doi: 10.1093/mnras/stt637

Ghisellini, G., Righi, C., Costamante, L., & Tavecchio, F. 2017, MNRAS, 469, 255, doi: 10.1093/mnras/stx806

Ghisellini, G., & Tavecchio, F. 2009, MNRAS, 397, 985, doi: 10.1111/j.1365-2966.2009.15007.x

Giommi, P., Padovani, P., Polenta, G., et al. 2012, MNRAS, 420, 2899, doi: 10.1111/j.1365-2966.2011.20044.x

Gokus, A., Paliya, V. S., Wagner, S. M., et al. 2021, A&A, 649, A77, doi: 10.1051/0004-6361/202039378

Gokus, A., Böttcher, M., Errando, M., et al. 2024, ApJ, 974, 38, doi: 10.3847/1538-4357/ad6a4e

Hayashida, M., Nalewajko, K., Madejski, G. M., et al. 2015, ApJ, 807, 79, doi: 10.1088/0004-637X/807/1/79

HI4PI Collaboration, Ben Bekhti, N., Flöer, L., et al. 2016, A&A, 594, A116, doi: 10.1051/0004-6361/201629178

Hook, I. M., & McMahon, R. G. 1998, MNRAS, 294, L7, doi: 10.1046/j.1365-8711.1998.01368.x

Houck, J. C., & Denicola, L. A. 2000, in Astronomical Data Analysis Software and Systems IX, ed. N. Manset, C. Veillet, & D. Crabtree, ASP Conf. Ser. No. 216 (San Francisco: Astron. Soc. Pacific), 591

Ighina, L., Caccianiga, A., Moretti, A., et al. 2024, A&A, 692, A241, doi: 10.1051/0004-6361/202451376
Inayoshi, K., Visbal, E., & Haiman, Z. 2020, ARA&A, 58, 27, doi: 10.1146/annurev-astro-120419-014455
Kaastra, J. S., & Bleeker, J. A. M. 2016, A&A, 587, A151, doi: 10.1051/0004-6361/201527395
Kamaram, S. R., Prince, R., Pramanick, S., & Bose, D. 2023, MNRAS, 520, 2024, doi: 10.1093/mnras/stad167
Keenan, M., Meyer, E. T., Georganopoulos, M., Reddy, K., & French, O. J. 2021, MNRAS, 505, 4726, doi: 10.1093/mnras/stab1182
Kreter, M., Gokus, A., Krauss, F., et al. 2020, ApJ, 903, 128, doi: 10.3847/1538-4357/abb8da
Liao, N.-H., Dou, L.-M., Jiang, N., et al. 2019, ApJL, 879, L9, doi: 10.3847/2041-8213/ab2893
Liao, N.-H., Li, S., & Fan, Y.-Z. 2018, ApJL, 865, L17, doi: 10.3847/2041-8213/aae20d
Lodato, G., & Natarajan, P. 2006, MNRAS, 371, 1813, doi: 10.1111/j.1365-2966.2006.10801.x
Lyke, B. W., Higley, A. N., McLane, J. N., et al. 2020, ApJS, 250, 8, doi: 10.3847/1538-4365/aba623
Madau, P., & Rees, M. J. 2001, ApJL, 551, L27, doi: 10.1086/319848
Marcotulli, L., Paliya, V., Ajello, M., et al. 2020, ApJ, 889, 164, doi: 10.3847/1538-4357/ab65f5
Marcotulli, L., Ajello, M., Urry, C. M., et al. 2022, ApJ, 940, 77, doi: 10.3847/1538-4357/ac937f
Marcotulli, L., Connor, T., Bañados, E., et al. 2025, arXiv e-prints, arXiv:2501.07637. https://arxiv.org/abs/2501.07637
Massaro, E., Giommi, P., Leto, C., et al. 2009, A&A, 495, 691, doi: 10.1051/0004-6361:200810161
Massaro, E., Maselli, A., Leto, C., et al. 2015, Ap&SS, 357, 75, doi: 10.1007/s10509-015-2254-2
Mattox, J. R., Bertsch, D. L., Chiang, J., et al. 1996, ApJ, 461, 396, doi: 10.1086/177068
McKinney, J. C., Tchekhovskoy, A., Sadowski, A., & Narayan, R. 2014, MNRAS, 441, 3177, doi: 10.1093/mnras/stu762
Medvedev, P., Sazonov, S., Gilfanov, M., et al. 2020, MNRAS, 497, 1842, doi: 10.1093/mnras/staa2051
Meyer, E. T., Fossati, G., Georganopoulos, M., & Lister, M. L. 2011, ApJ, 740, 98, doi: 10.1088/0004-637X/740/2/98
Meyer, M., Scargle, J. D., & Blandford, R. D. 2019, ApJ, 877, 39, doi: 10.3847/1538-4357/ab1651
Migliori, G., Siemiginowska, A., Sobolewska, M., et al. 2023, MNRAS, 524, 1087, doi: 10.1093/mnras/stad1959
Moretti, A., Ghisellini, G., Caccianiga, A., et al. 2021, ApJ, 920, 15, doi: 10.3847/1538-4357/ac167a
Nalewajko, K., & Gupta, M. 2017, A&A, 606, A44, doi: 10.1051/0004-6361/201731329
Nasa High Energy Astrophysics Science Archive Research Center (Heasarc). 2014, HEAsoft: Unified Release of FTOOLS and XANADU, Astrophysics Source Code Library, record ascl:1408.004
Nieppola, E., Valtaoja, E., Tornikoski, M., Hovatta, T., & Kotiranta, M. 2008, A&A, 488, 867, doi: 10.1051/0004-6361:200809716
Pacciani, L., Tavecchio, F., Donnarumma, I., et al. 2014, ApJ, 790, 45, doi: 10.1088/0004-637X/790/1/45
Paliya, V. S., Ajello, M., Cao, H. M., et al. 2020, ApJ, 897, 177, doi: 10.3847/1538-4357/ab9c1a
Paliya, V. S., Domínguez, A., Ajello, M., Olmo-García, A., & Hartmann, D. 2021, ApJS, 253, 46, doi: 10.3847/1538-4365/abe135
Paliya, V. S., Parker, M. L., Fabian, A. C., & Stalin, C. S. 2016, ApJ, 825, 74, doi: 10.3847/0004-637X/825/1/74
Paliya, V. S., Ajello, M., Ojha, R., et al. 2019, ApJ, 871, 211, doi: 10.3847/1538-4357/aafa10
Planck Collaboration, Ade, P. A. R., Aghanim, N., et al. 2016, A&A, 594, A13, doi: 10.1051/0004-6361/201525830
Prandini, E., & Ghisellini, G. 2022, Galaxies, 10, doi: 10.3390/galaxies10010035
Richards, G. T., Strauss, M. A., Fan, X., et al. 2006, AJ, 131, 2766, doi: 10.1086/503559
Richards, G. T., Myers, A. D., Gray, A. G., et al. 2009, ApJS, 180, 67, doi: 10.1088/0067-0049/180/1/67
Sahakyan, N., Israyelyan, D., Harutyunyan, G., Khachatryan, M., & Gasparyan, S. 2020, MNRAS, 498, 2594, doi: 10.1093/mnras/staa2477
Sbarrato, T., Ghisellini, G., Tagliaferri, G., et al. 2015, MNRAS, 446, 2483, doi: 10.1093/mnras/stu2269
—. 2022, A&A, 663, A147, doi: 10.1051/0004-6361/202243569
Schmidt, G. D., Elston, R., & Lupie, O. L. 1992, AJ, 104, 1563, doi: 10.1086/116341
Schneider, D. P., Hall, P. B., Richards, G. T., et al. 2007, AJ, 134, 102, doi: 10.1086/518474
Sexton, R. O., Secrest, N. J., Johnson, M. C., & Dorland, B. N. 2022, ApJS, 260, 33, doi: 10.3847/1538-4365/ac609f
Shakura, N. I., & Sunyaev, R. A. 1973, A&A, 24, 337
Shen, Y., Richards, G. T., Strauss, M. A., et al. 2011, ApJS, 194, 45, doi: 10.1088/0067-0049/194/2/45
Shimwell, T. W., Hardcastle, M. J., Tasse, C., et al. 2022, A&A, 659, A1, doi: 10.1051/0004-6361/202142484
Sądowski, A., Narayan, R., McKinney, J. C., & Tchekhovskoy, A. 2014, MNRAS, 439, 503, doi: 10.1093/mnras/stt2479

Smith, P. S. 2016, Galaxies, 4, 27, doi: 10.3390/galaxies4030027

Smith, P. S., Jannuzi, B. T., & Elston, R. 1991, ApJS, 77, 67, doi: 10.1086/191598

Smith, P. S., Williams, G. G., Schmidt, G. D., Diamond-Stanic, A. M., & Means, D. L. 2007, ApJ, 663, 118, doi: 10.1086/517992

Tomsick, J., Zoglauer, A., Sleator, C., et al. 2019, in Bulletin of the American Astronomical Society, Vol. 51, 98, doi: 10.48550/arXiv.1908.04334

Tomsick, J., Boggs, S., Zoglauer, A., et al. 2024, in 38th International Cosmic Ray Conference, 745, doi: 10.48550/arXiv.2308.12362

Truemper, J. 1982, Advances in Space Research, 2, 241, doi: 10.1016/0273-1177(82)90070-9

Urry, C. M., & Padovani, P. 1995, PASP, 107, 803, doi: 10.1086/133630

Veres, P., Frey, S., Paragi, Z., & Gurvits, L. I. 2010, A&A, 521, A6, doi: 10.1051/0004-6361/201014957

Verner, D. A., Ferland, G. J., Korista, K. T., & Yakovlev, D. G. 1996, ApJ, 465, 487, doi: 10.1086/177435

Volonteri, M., Haardt, F., Ghisellini, G., & Della Ceca, R. 2011, MNRAS, 416, 216, doi: 10.1111/j.1365-2966.2011.19024.x

Volonteri, M., Haardt, F., & Madau, P. 2003, ApJ, 582, 559, doi: 10.1086/344675

Wang, F., Yang, J., Fan, X., et al. 2021, ApJL, 907, L1, doi: 10.3847/2041-8213/abd8c6

Watson, M. G., Schröder, A. C., Fyfe, D., et al. 2009, A&A, 493, 339, doi: 10.1051/0004-6361:200810534

Whalen, D. J., & Fryer, C. L. 2012, ApJL, 756, L19, doi: 10.1088/2041-8205/756/1/L19

Wilms, J., Allen, A., & McCray, R. 2000, ApJ, 542, 914, doi: 10.1086/317016

Wise, J. H., Regan, J. A., O'Shea, B. W., et al. 2019, Nature, 566, 85, doi: 10.1038/s41586-019-0873-4

Wolf, J., Salvato, M., Belladitta, S., et al. 2024, A&A, 691, A30, doi: 10.1051/0004-6361/202451035

Wood, M., Caputo, R., Charles, E., et al. 2017, in International Cosmic Ray Conference, Vol. 301, 35th International Cosmic Ray Conference (ICRC2017), 824, doi: 10.22323/1.301.0824

Worsley, M. A., Fabian, A. C., Celotti, A., & Iwasawa, K. 2004, MNRAS, 350, L67, doi: 10.1111/j.1365-2966.2004.07887.x

Worsley, M. A., Fabian, A. C., Pooley, G. G., & Chandler, C. J. 2006, MNRAS, 368, 844, doi: 10.1111/j.1365-2966.2006.10173.x

Yu, Q., & Tremaine, S. 2002, MNRAS, 335, 965, doi: 10.1046/j.1365-8711.2002.05532.x

Zhang, Y., An, T., & Frey, S. 2020, Science Bulletin, 65, 525, doi: 10.1016/j.scib.2020.01.008

Zhou, B., Dai, B., & Yang, J. 2021, PASJ, 73, 850, doi: 10.1093/pasj/psab051

Zombeck, M. V., David, L. P., Harnden, F. R., & Kearns, K. 1995, in Society of Photo-Optical Instrumentation Engineers (SPIE) Conference Series, Vol. 2518, EUV, X-Ray, and Gamma-Ray Instrumentation for Astronomy VI, ed. O. H. Siegmund & J. V. Vallerga, 304–321, doi: 10.1117/12.218385